Oelze, M., von Blanckenburg, F., Bouchez, J., Hoellen, D., Dietzel, M. (2015): The effect of Al on Si isotope fractionation investigated by silica precipitation experiments. - *Chemical Geology*, *397*, p. 94-105.

DOI: http://doi.org/10.1016/j.chemgeo.2015.01.002

The effect of Al on Si isotope fractionation investigated by silica precipitation experiments

Marcus Oelze*[a], Friedhelm von Blanckenburg[a,c], Julien Bouchez[a], Daniel Hoellen[b], Martin Dietzel[b]

[a] *Helmholtz Centre Potsdam, GFZ German Research Centre for Geosciences;*
[*] *Corresponding author: oelze@gfz-potsdam.de*
[b] *Institute of Applied Geosciences, Graz University of Technology*
[c] *Department of Geoscience, Freie Universität Berlin*

Abstract

Mass-dependent isotope fractionation occurring during precipitation of solids in low-temperature environments often depends on precipitation rate. Using a series of precipitation experiments in which continuous precipitation and dissolution of Si solids is forced by daily cyclic freezing (solid formation) and thawing (solid re-dissolution), we show this dependence. We conducted six Si precipitation experiments for about 120 days with initial dissolved Si concentration of 1.6 mmol/l Si, at pH values between 4.5 and 7, with additions of 0.1 - 1 mM of dissolved aluminium (Al), and in the absence of Al. During all experiments increasing amounts of an X-ray amorphous silica-containing solid are formed. No Si isotope fractionation occurs during formation of almost pure Si solids, interpreted as an absence of Si isotope fractionation during polymerization of silicic acid. Si isotope fractionation occurs only in the high-Al concentration experiments, characterized by an enrichment of the light Si isotopes in the solids formed early. With ongoing duration of the experiments, a re-dissolution of these solids is indicated as the Si isotope

value of the complementary solution shifts to lighter values and eventually reaches near-initial compositions. Hence, our high-Al experiments are characterized by a gradual shift from a regime that is dominated by unidirectional kinetic isotope fractionation with solids formed that are up to 5‰ lighter in their $^{30}Si/^{28}Si$ ratio than the corresponding solution, to one of steady-state between dissolution and precipitation with the $^{30}Si/^{28}Si$ ratio of the solid being almost identical to the solution ($\Delta_{\text{solid-solution}} \approx 0‰$). This suggests that the enrichment of light Si isotopes found in natural environments is caused exclusively by a unidirectional kinetic isotope effect during fast precipitation of solids, aided by co-precipitation with Al phases or other carrier phases (e.g. Fe(III)). By contrast, during slow precipitation, or in the absence of a carrier phase like Al, no Si isotope fractionation is expected and solids obtain the composition of the ambient fluid.

Keywords: isotope fractionation, stable silicon isotopes, silicon precipitation, kinetic fractionation, reaction rate-dependence

---

1. Introduction

Ratios of stable isotopes of Si have emerged as a powerful proxy to distinguish the reactions involved in low-temperature water-mineral and water-rock interaction. The isotope ratios potentially trace the way Si is released from Si-bearing solids into soil and (diagenetic) interstitial solutions. Si isotopes also trace how silica is precipitated into secondary solids from these solutions. Given the useful information Si stable isotopes provide along this pathway, the resulting isotope ratios have been increasingly explored as a tool to trace silicate weathering, sediment diagenesis and the associated silicifica-

tion, precipitation of siliceous sediments from hydrothermal vents, and the genesis of Precambrian cherts and banded iron formation (e.g. Ziegler et al. (2005a); Robert and Chaussidon (2006); Steinhoefel et al. (2009); van den Boorn et al. (2010); Chakrabarti et al. (2012)). In general, dissolved Si in soil and in river waters is enriched in the heavy isotopes as compared to the primary silicate minerals where Si is sourced from. The corresponding isotopically light reservoir is found in secondary siliceous solid phases (Ziegler et al., 2005a,b; Georg et al., 2007; Opfergelt et al., 2009; Bern et al., 2010; Steinhoefel et al., 2011). Furthermore, siliceous precipitates from hydrothermal solutions enriched in dissolved Si also show the common picture of preferential incorporation of light isotopes in the precipitates (Douthitt, 1982; Ding et al., 1996; de La Rocha et al., 2000). This pictures is also inferred from the prevalence of low isotope ratios in Precambrian cherts (Andre et al., 2006; Steinhoefel et al., 2009, 2010; van den Boorn et al., 2010). However, for chert formation, the way in which diagenetic silicification modifies the Si isotope composition from that of the original deposits is far from understood. Basile-Doelsch et al. (2005) found some of the lowest Si isotope ratios in Aptian siliceous cements. Chen et al. (2007) also reported low isotope ratios in *Anabarites celoms* (tubular small shelly fossil), and in quartz ocurring in granular phosphates. In contrast, Robert and Chaussidon (2006), Abraham et al. (2011) and Chakrabarti et al. (2012) reported Archean cherts enriched in heavy Si isotopes.

Converting these observations into a quantitative understanding of the movement of silica in low-temperature environments requires knowledge of the isotope fractionation factors associated with precipitation and recrystallization

of siliceous solids. However, not only do we lack even first–order experimental estimates of equilibrium isotope fractionation factors, but probably the formation of many siliceous secondary minerals and chemical deposits is affected by non-equilibrium processes, as they are often enriched in light Si isotopes which suggest that the origin of the Si isotope fractionation is mostly kinetic (see e.g. Ziegler et al. (2005a); Georg et al. (2009); DePaolo (2011)). In these conditions, the relative importance of the forward (precipitation) and backward (dissolution) reaction rates determine the net solid formation rate and the associated isotope fractionation factor (DePaolo, 2011). In addition, sedimentary silicates usually do not directly precipitate from aqueous solutions, as documented by the large number of known amorphous silica precursor phases (e.g. Iler (1979)). Therefore the generation of surface area during nucleation, growth and dissolution, and precursor replacement is important as the processes and rates at the mineral-water interface control the isotope composition of the solid material during mineral growth (Cole et al., 1983; Criss et al., 1987; Steefel and Van Cappellen, 1990; Nielsen et al., 2012; Druhan et al., 2013).

To date, only a few notable studies have explored Si isotope fractionation during the fixation of Si from solution under controlled experimental conditions. The Si isotope fractionation during adsorption of Si onto Fe-oxides, the Si isotopic evolution during allophane- and gel-like solid formation and the Si isotope fractionation during abiotic silica precipitation at low temperatures have been experimentally investigated (Li et al., 1995; Ziegler et al., 2005a; Delstanche et al., 2009; Opfergelt et al., 2009; Geilert et al., 2014). Recently, silicon isotope fractionation during adsorption of Si onto Al-hydroxides has

been shown to result in a strong rate dependence of silicon isotope fractionation (Oelze et al., 2014). All these studies demonstrate the preferential incorporation of ^{28}Si into the solid, most likely during Si adsorption onto the solid phase. Isotope fractionation factors $10^3 ln\alpha_{\text{solid/solution}}$ range from -1.0‰ to -1.6‰ for adsorption of Si onto Fe-oxides, -1.8‰ up to -3‰ for adsorption of Si onto Al-hydroxides and up to $\approx$ -3.0‰ for precipitation of allophane- and gel-like solid phases. First-principle calculations predict an enrichment of ^{30}Si in the higher-ordered solid at equilibrium conditions (Ding et al., 1996; Méheut et al., 2007, 2009). However, these predictions suggest that the Si isotope fractionation of the aforementioned experimental studies are dominated by a kinetic isotope effect. Indeed, attaining Si isotopic equilibrium in experimental settings is virtually impossible due to the extremely low exchange rates between solids and fluids in low-temperature processes, especially in the SiO_2-H_2O system. Li et al. (2011) suggested that recrystallization (or re-organization) induced by "Ostwald ripening", the dissolution of small particles and the re-deposition of the dissolved species on the surfaces of larger particles in a saturated solution, is the only way to induce an isotope exchange at low temperature that is not overprinted by kinetic processes. To test whether equilibrium has indeed been attained, experimentalists use the addition of isotopically-enriched species in one of the two compartments (Johnson et al., 2002; Welch et al., 2003; Schuessler et al., 2007). However, this approach is not possible if, as is the case here, Si is precipitated from a homogeneous solution.

A possible experimental approach in which dissolution-precipitation reactions take place is a batch reactor in which solid precipitation is driven by

evaporation of the fluid, and solid dissolution driven by dilution of the fluid. However, the slow evaporation rates involved in such an experiment would result in excessively long experimental runtimes. For Si-containing solids, once precipitated, isotopic equilibration times will exceed any feasible experimental runtime due the slow exchange rates. It is most likely that dissolution is the limiting step to reach full exchange between formed solid products and solution. The low dissolution rate for amorphous silica ($\approx 1 * 10^{-12}$ mol$*$m$^{-2}*$sec^{-1} at 20°C; Icenhower and Dove (2000)) will likely impair attainment of equilibrium as in experiments of $CaCO_3$ precipitation (Tang et al., 2008).

To circumvent these difficulties we designed a novel approach. Alternating dissolution-precipitation, implying depolymerization-polymerization of silica, is induced by freezing and thawing for predefined cycle length over a long run duration (Dietzel, 2005). During freezing, only H_2O molecules are captured in the ice lattice and the remaining solution becomes supersaturated in Si and precipitation of solids from the remaining solution occurs as soon as a critical supersaturation is reached. At the end of the freezing time span, temperatures are increased and the ice previously formed melts. Hence the solution is then undersaturated with respect to the formed solids, leading to their partial dissolution during thawing. By continuing these freeze-thaw cycles steady-state conditions between silica precipitation and dissolution are reached, meaning that the dissolution and precipitation fluxes compensate each other at the scale of a freeze-thaw cycle. At this stage concentrations of dissolved Si do not change from a freeze-thaw cycle to the next. Our setup allows us to explore the temporal change in the Si isotope fractionation factor

as the system evolves from a state that is characterized by high net Si removal rates (dominated by unidirectional kinetic isotope fractionation), to a state where the net change for precipitation and dissolution is close to zero.

The rationale for this approach becomes apparent from fundamental experimental studies on dissolution-precipitation kinetics of SiO_2 polymorphs. The process of dissolution and precipitation of SiO_2 polymorphs has been described as fully reversible (Rimstidt and Barnes, 1980; Renders et al., 1995; Carroll et al., 1998). Using the empirical relationships of Rimstidt and Barnes (1980) and Dove et al. (2008) for the dependence of the dissolution rate on temperature and saturation state we can estimate the dissolution rate for an experiment maintained far from equilibrium. The dissolution rate and therefore the time needed to reach full exchange is accelerated by a factor of 60 in comparison to experiments close to equilibrium conditions.

Our experimental approach also provides insight into the numerous geological processes associated with water-solid interaction that involve repeated dissolution-precipitating cycles of silica at the water-solid interface, such as for example during mineral replacement in weathering reactions, diagenesis, silicification, or biogenic ooze maturation. In addition, this experimental approach of repeated freeze-thaw cycles can give insights into the formation process of authigenic silicates in polar regions (Tedrow, 1966; Dickinson and Grapes, 1997).

However, in virtually all Earth surface reactions will Si release from primary silicates be accompanied by variable amounts of Al. Reactions between Si and Al are hence likely the first crucial reactions. Aluminum in the system not only reduces the solubility of Si in aqueous solutions (Dixit et al., 2001;

Van Cappellen et al., 2002), it also further provides surface area for fast adsorption of Si (Hingston and Raupach, 1967; Dietzel and Böhme, 1997). In addition, pH will exert a first-order control over the precipitation kinetics of both elements as the solubility of Al and Si are both "pH dependent". Therefore, we performed experiments of Si precipitation from solutions in the presence of variable Al concentrations and different pH.

In the present study, we conducted six Si precipitation experiments for about 120 days with initial dissolved Si concentration of 1.6 mmol/l Si, with additions of different amounts of Al (0, 0.1, 1 mmol/l dissolved Al) and explored the evolution of the dissolved silicon isotope composition. In all experiments increasing amounts of an X-ray amorphous silica-containing solids are formed. The evolution of the dissolved silicon isotope composition can be explained by the presence or absence of dissolved Al.

2. Framework for isotope fractionation during precipitation

Because of the diversity of isotope fractionation mechanisms encountered in our experiments, we first review the framework of definitions of these processes. There are several processes during which kinetic isotope fractionation might occur, for example diffusion, evaporation, or due to differences in energy barriers. In the literature, the term "kinetic" actually serves as an umbrella for two fundamentally different processes generating isotope fractionation: (1) differential transport velocity of isotopes over a given distance for example during diffusion ("transport-limited") and (2) differences in the energetic barrier associated with chemical reactions ("reaction-limited").

In "transport-limited" regimes, kinetic isotope fractionation arises from dif-

ferent transport velocities (e.g. different diffusion coefficients) resulting from the mass differences of isotopes (Richter et al., 2006). This regime will not be further discussed in this paper, as under our experimental conditions this effect will be small (see Table 1 in Richter et al. (2006)). In addition to isotope fractionation due to different diffusion coefficients for isotopes, the influence of a chemical gradient in solution without sufficient stirring must be considered possible (Gislason and Oelkers, 2003). Such an effect is also described as "transport-limited". The observed precipitation and dissolution rates and further the measured isotope fractionation are then influenced by the evolution of a chemical gradient and are no longer dependent on the bulk fluid chemistry but rather on the evolution of the chemical gradient. It is assumed here that mixing of the solution due to ice movement and climate cabinet vibrations will preclude the effects of chemical gradients and can be therefore considered as subordinate.

In the "reaction-limited" case the kinetic effect arises because an activation energy has to be overstepped to form or break bonds. The activation energy is likely to differ between isotopes of an element, as bonds with heavier isotopes have lower zero point energies than light isotopes (Urey, 1947). For example, during ion desolvation kinetic isotope fractionation has been documented to be induced by the difference in activation energy (Hofmann et al., 2012). The Arrhenius equation indicates that at a given temperature, the reaction rate constant of light isotopes is higher than that of heavy isotopes. Importantly, during a reversible reaction the light isotope will be favored in both directions of the reaction. Therefore it follows that the overall isotope fractionation is governed by the relative magnitudes of forward and backward reaction

rates, and by the individual isotope fractionation factors for these reactions (DePaolo, 2011).

3. Materials and Methods

3.1. Description of Experiments

Freeze-thaw experiments were conducted following a method adapted from Dietzel (2005). All experiments were carried out at similar initial Si concentrations and at two pH conditions (near neutral: pH 7 and acidic: pH 4.5 or 5) to mimic typical soil pH values (Schwertmann and Fischer, 1982). Three experimental series were conducted: the first series (a) was carried out without Al addition, the second series (b) with low amounts Al added (low: 0.1 mmol/l Al) and the third series (c) with high Al amounts added (high: 1 mmol/l Al), respectively. All reagent solutions were at least of analytical grade, and Milli-Q water (18.2 $M\Omega$) was used. The pH of the initial solutions was adjusted with diluted HCl and NaOH. Initial solutions of 1.6 mmol/l Si were prepared from a tetraethylorthosilicate (TEOS) solution acquired from Merck. Aluminum was added as $AlNO_3{*}9H_2O$ and 100 ml of these initial solutions were then evenly distributed into each of several 100 ml polyethylene (PE) bottles. One separate bottle was prepared for each experimental runtime (each data point in Figures 1, 2, 5 and 6 is an individual bottle; see also Tables 1, 2 and 3) and was removed for analyses after a given of runtime.

We conducted the cyclic freeze-thaw experiments in a climate cabinet where temperature was changed over 24 hour-cycles from 20℃ to -20℃ (6 h from 20℃ to -20℃, 6 h at -20℃, 6 h from -20℃ to 20℃, 6h at 20℃; heating and cooling rate: 0.11℃ min^{-1}). About 4 h after reaching 0℃ visual inspection

showed that the experimental solution was completely frozen or thawed, respectively, but nevertheless small amounts of unfrozen water might still be present even at -20℃ (e.g. Anderson and Tice (1973); Anderson (1981)). During freezing, the formation of ice crystals results in a decrease of the remaining volume of the solution and therefore an elevated concentration of dissolved Si in the solution. Further the decrease in temperature leads to a decrease in the amorphous Si solubility (Rimstidt and Barnes, 1980). Both effects induce supersaturation with respect to amorphous silica so that precipitation of amorphous silica can occur. During warming of the solution and subsequent thawing of ice crystals, the solution becomes undersaturated with respect to the formed Si-containing solids which are expected to partly redissolve. The amount of silica that is precipitated from solution at a given time interval depends on the rate of ice formation and the kinetics of silica precipitation (see Dietzel (2005) and references therein). Temperature limits, rates of cooling and warming, total solution volume and the initial concentration of dissolved Si are decisive experimental parameters. We performed several pre-experiments to find these parameters. The cooling and thawing rates were set to 0.11℃ min^{-1}, a rate at which we observed that precipitation of Si starts ca. 0.5 hours before the solution is completely frozen.

Freeze-thaw cycles were repeated up to 130 times. Although the solutions were not stirred or shaken, we assume that the solution was sufficiently well mixed through the motions of the ice crystals. During the thawing period, the melt water accumulated at the bottom of the bottles and the residual ice at the top. Additionally, vibration of the climate cabinet due to ventilation enhanced mixing. Therefore isotope fractionation due to diffusion

(Richter et al., 2006) can be regarded as negligible. We cannot fully exclude the effect of "transport-limitation" that arises from a chemical gradient (surrounding the particles formed; see Gislason and Oelkers (2003) and Section 2). This effect will only affect the reaction rates and therefore the resulting isotope fractionation factors but will not change the reaction mechanism itself. Therefore the derived isotope fractionation mechanisms do not depend on this.

3.2. Requirements for Si precipitation experiments

3.2.1. Si initial concentration

The precipitation of amorphous silica requires high concentrations of dissolved Si ($\gg$ 2 mmol/l Si at 25°C, the solubility of amorphous silica (Gunnarsson and Arnorsson, 2000)). In addition, as we aimed to analyze both the dissolved Si and the precipitated silica for their Si isotope composition, a significant amount of solid Si has to be formed. Therefore the dissolved Si has to be prepared with even higher Si concentrations than required for the first nucleation. However, it is a requirement that no polymeric Si is present in the experimental initial solution, as its presence would render isotope data interpretation unnecessarily complex. To avoid formation of polysilicic acid, the Si concentration of the initial solution was kept below the solubility of amorphous silica. An initial Si concentration of 1.6 mmol/l was deemed sufficient to meet this requirement. Initial solutions were analyzed for the polymerization degree of dissolved Si (β-silicomolybdate method; see Online Supplement A and for further details Iler (1979) and Dietzel (2000)) by measuring the total Si concentration using ICP-OES and subtracting the concentration of monosilicic acid determined by the β-silicomolybdate method.

The results showed that no colloidal Si was present in the initial solution in any of the experiments.

3.2.2. Si source

We used tetraethylorthosilicate (TEOS) as a Si source. Dietzel (1993, 2002) showed that when using TEOS as Si source only monomeric silicic acid is formed below the solubility of amorphous silica and that the behavior of dissolved Si in experiments is identical to monomeric silicic acid solutions that were prepared by alternative means (e.g. dissolution of silicates). One further advantage of TEOS is that no associated cations of other minor elements (that would be released during the dissolution of other Si sources, such as silicates (e.g. Na_2SiO_3) or alkaline standard solutions (SiO_2 in 2% NaOH)) are present in the solution. These elements would then have to be removed to obtain pure silicic acid for the experiments. Further the solution can be easily produced by adding small volumes of TEOS to water where it converts into silicic acid via a hydrolysis reaction. However, the side product of this reaction is ethanol that we estimate to be present in our experimental solution at a concentration of 6.4 mmol/l. We explored whether the ethanol potentially remaining in the purified mass spectrometric solutions induces analytical artifacts during the preparation and measurement of Si isotopes by measuring the purified solutions and the precipitated solid counterpart of the conducted experiments (see Table 3). Mass balance shows that each fluid-solid pair yields a calculated bulk isotopic composition that is identical to that of the initial solution. The fact that the calculated bulk isotope composition of the system at different fluid-solid ratios (mass dissolved Si/mass of precipitated silica) is similar to the composition of the initial solution

demonstrates the absence of analytical artifacts induced by the release of ethanol during preparation of Si-containing solutions using TEOS.

3.3. Filtration of solutions and chemical separation for Si isotope analyses

The precipitate was separated from the solution by using cellulose acetate filters (0.1 μm). Where sufficient amounts of precipitate were obtained, the precipitate was rinsed off from the filter and dried at 40°C. The filtered precipitates of freeze-thawing experiments were digested ($\approx$ 2 mg sample) using 200 μl 1M NaOH (analytical grade; Si concentration <1 ppb) in Teflon beakers. After digestion, samples were taken up in Milli-Q water for column chemistry. Si was separated from the matrix following the method of Georg et al. (2006b): the filtered solutions and the digested precipitates were loaded onto pre-cleaned columns (1.5 ml of BioRad DOWEX 50W-X8; 200-400 mesh) and Si was eluted with 5 ml Milli-Q water and stored in pre-cleaned centrifuge tubes. It was assured for all samples that the Si yield was >95%, which was checked by ICP-OES (Varian 720-ES).

3.4. Mass spectrometry

Determination of Si isotopic composition was usually done in medium resolution mode on a Thermo Neptune multi-collector inductively coupled mass spectrometer (MC-ICP-MS). The purified sample solutions were introduced into the plasma using the Thermo stable introduction system (SIS) glass spray chamber (wet-plasma) equipped with a 120 μl/min nebulizer. Samples measured in wet plasma conditions were diluted to 2.5 ppm in 0.1 M HCl which typically resulted in an intensity of 5 V/ppm on ^{28}Si (10^{11} Ω

resistor). To correct for instrumental mass bias, we used a standard-sample-bracketing procedure. Measurements were conducted on the interference-free low-mass side of the three Si isotopes. Samples and secondary standards were measured at least 4 times during a sequence; each sample or standard was measured for 30 cycles with an integration time for each cycle of 4 s. Pure 0.1 M HCl solutions were measured before and after each standard-sample-standard block and were used for on-peak zero correction. Typical intensities of ^{28}Si in blank solutions were below 5 mV. We report Si isotope data relative to the standard reference material NBS28 (quartz sand) in the delta notation according to Coplen (2011) as $\delta(^{29/28}\mathrm{Si})_{\mathrm{NBS28}}$ and $\delta(^{30/28}\mathrm{Si})_{\mathrm{NBS28}}$ expressed in per mill (‰) by multiplication of Equation 1 and 2 with a factor of 10^3:

$$\delta(^{29/28}\mathrm{Si})_{\mathrm{NBS28}} = \left(\frac{\left(\frac{^{29}\mathrm{Si}}{^{28}\mathrm{Si}}\right)_{\mathrm{sample}}}{\left(\frac{^{29}\mathrm{Si}}{^{28}\mathrm{Si}}\right)_{\mathrm{NBS28}}} - 1 \right) \tag{1}$$

$$\delta(^{30/28}\mathrm{Si})_{\mathrm{NBS28}} = \left(\frac{\left(\frac{^{30}\mathrm{Si}}{^{28}\mathrm{Si}}\right)_{\mathrm{sample}}}{\left(\frac{^{30}\mathrm{Si}}{^{28}\mathrm{Si}}\right)_{\mathrm{NBS28}}} - 1 \right) \tag{2}$$

Reported errors on delta values are the 95% confidence interval (CI) were calculated according to Eq.3:

$$\mathrm{CI} = \overline{\delta(^{x/28}\mathrm{Si})_{\mathrm{NBS28}}} \pm \mathrm{t_{n\text{-}1}} \times \mathrm{SE} \tag{3}$$

where $\overline{\delta(^{x/28}\mathrm{Si})_{\mathrm{NBS28}}}$ is the mean of the measured delta values with x= ^{29}Si or ^{30}Si for the sample or standard (at least n=4), $\mathrm{t_{n\text{-}1}}$ is a critical value from tables of the *Student's t*-law and SE is the standard error of the mean. Two

reference materials (BHVO-2 and IRMM-017) were used to control accuracy of our measurements. These two standards measured over 12 months and after several individual digestion and chemical separation procedures (digestion and Si separation procedure adapted from Georg et al. (2006b) and Zambardi and Poitrasson (2011)) yielded for BHVO-2g: $\delta(^{30/28}\mathrm{Si})_{\mathrm{NBS28}}$ = -0.27 ± 0.02 ‰ (n=73) and for IRMM-017 $\delta(^{30/28}\mathrm{Si})_{\mathrm{NBS28}}$ = -1.36 ± 0.03 ‰ (n=53). The obtained values of both secondary standards are comparable, within uncertainty, to those reported in the literature for BHVO-2g $\delta(^{30/28}\mathrm{Si})_{\mathrm{NBS28}}$ = -0.28 ± 0.02 ‰ (Reynolds et al., 2007; Fitoussi et al., 2009; Savage et al., 2010; Zambardi and Poitrasson, 2011; Armytage et al., 2011) and IRMM-017 $\delta(^{30/28}\mathrm{Si})_{\mathrm{NBS28}}$ = -1.29 ± 0.10 ‰ (Ding et al., 1996; Coplen et al., 2002; Chmeleff et al., 2008).

4. Results

Si and Al concentration as well as $\delta(^{29/28}\mathrm{Si})_{\mathrm{NBS28}}$ and $\delta(^{30/28}\mathrm{Si})_{\mathrm{NBS28}}$ values for the freeze-thaw experiments are reported in Tables 1, 2 and 3.

4.1. Si and Al concentrations

The evolution of dissolved Si and Al concentrations with time is displayed in Figures 1 and 2, respectively. X-ray diffraction patterns (XRD, Panalytical X'Pert Pro, Co-Kα) show that the formed precipitates are not crystalline (Figure 3). Si concentration decreases with runtime in all experiments. In the zero-Al experimental series (a) a pure Si-containing solid is formed. In the low-Al experimental series (b) (0.1 mmol/l Al) and in the high-Al experimental series (c) (1 mmol/l Al), a Si and Al-containing solid is formed (see Figures 1, 2 and 4).

The zero-Al experimental series (a) shows low Si removal rates and low amounts of solid precipitated. The low-Al experimental series (b) (0.1 mmol/l Al) shows lower removal rates of dissolved Si than the high-Al experimental series (c) (1 mmol/l Al). At acidic conditions, the zero-Al experimental series (a) shows higher Si removal rates from solution and larger amounts of Si precipitated than at neutral pH conditions. In the low-Al experimental series (b) (0.1 mmol/l Al), the removal of Si is instead more pronounced and rapid at neutral pH conditions. The highest removal rates are observed in the high-Al experimental series (c) (1 mmol/l Al), for the experiments at pH 7, where almost all Si (>95%) is removed during the first 10 days (see Figures 1 and 2). For comparison, in the low-Al experiment (0.1 mmol/l Al) conducted at pH 4.5 only minor amounts (<5%) of Si were removed from the

solution during the first 60 days. The high-Al experiments (1 mmol/l Al) at pH 4.5 and the low-Al experiment (0.1 mmol/l Al) at pH 7 show similar behavior in the evolution of their Si concentrations. After 50 days, more than 50% of the initial amount of dissolved Si was removed from solution. Finally, the low-Al experiment (0.1 mmol/l Al) at pH 7 shows an increase in dissolved Si concentration between day 80 and 100. As each data point corresponds to an individual experiment, irregularities in the preparation of a particular sample might have resulted in such a deviation.

Dissolved Al concentrations decrease with time in most Al-containing experiments, except for the low-Al experiment at pH 4.5. The evolution of Al concentration strongly depends on the pH value and the initial Al concentration (Figure 2). In the low-Al experiment (0.1 mmol/l Al; series (b)) at pH 4.5, the Al concentration remains constant during the entire experiment (see Figure 2). This contrasts with the low-Al experiment (0.1 mmol/l Al; series (b)) at pH 7, where the Al concentration declines continuously during the first 50 days, until all Al is completely removed from solution. For the high-Al experiment (1 mmol/l Al; series (c)) at pH 4.5, the Al concentration declines during the first 20 days to 0.6 mmol/l and stabilizes around this concentration for the remaining experimental runtime. At pH 7 in the high-Al experiment (1 mmol/l Al; series (c)), all Al was almost quantitatively removed from the solution.

Analysis of dissolved Al concentrations of the respective initial solutions for the high-Al experiment at pH 7 (1 mmol/l Al) at 25°C indicates substantial precipitation of Al immediately after adding Al even before starting the freeze-thaw cycles. This can be explained by $Al(OH)_3$ formation due to

high supersaturation with respect to amorphous $Al(OH)_3$. To confirm this hypothesis we used the computer code PHREEQC (Parkhurst and Appelo, 1999) to model saturation indices (SI) with respect to amorphous $Al(OH)_3$. The saturation index is calculated by dividing the chemical activities of the dissolved ions of the mineral (ion activity product, IAP) by their solubility product (K_{sp}), such that S.I. = $\log(IAP/K_{sp})$. The calculated saturation indexes (S.I.(amorphous $Al(OH)_3$)) for the low-Al experimental series (b) (0.1 mmol/l Al) are -2.12 and 0.73 (for the reference solutions at 25℃) at a pH of 4.5 and 7, respectively. For the high-Al experimental series (c) (1 mmol/l Al) saturation indexes S.I.(amorphous $Al(OH)_3$) of -1.13 and 1.73 are predicted for the reference solutions at 25℃ at a pH of 4.5 and 7, respectively. Precipitation of Al (and Si) prior to cyclic freezing is only observed for the high-Al experiment (1 mmol/l Al) at pH 7. For the low-Al experiment (0.1 mmol/l Al) at pH 7 the calculation suggests that the solution is also supersaturated with respect to amorphous $Al(OH)_3$, but no precipitation occurs at room temperature.

We calculated the evolution of the Si/Al ratio of the solid (Si/Al_{solid}) with time (Figure 2). The Si/Al_{solid} ratio remains constant at ≈1.5 throughout the experimental runtime for the high-Al experiment (1 mmol/l Al; series (c)) conducted at pH 7. For the high-Al experiment (1 mmol/l Al; series (c)) conducted at pH 4.5, Si/Al_{solid} evolves from ≈1 to ≈2.5. For the low-Al experiments (0.1 mmol/l Al; series (b)), Si/Al_{solid} shows a pronounced increase with time from ratios of ≈0.1 to ≈15.

406 *4.2. Silicon isotopes*

407 We present Si isotope ratios measured in solution reported as $\Delta(^{30/28}Si)_{solution} =$
408 $\delta(^{30/28}Si)_{solution(t)} - \delta(^{30/28}Si)_{solution(initial)}$ (see Figure 5 and Figure 6). Cor-
409 responding precipitates were also analyzed for the high-Al experiment (1
410 mmol/l Al; series (c)) at pH 4.5 (see Table 3). Mass balance shows that pre-
411 cipitates yield the complementary isotope reservoir to the dissolved phase.

412 For the zero- and low-Al experimental series (a) and (b), at both pH val-
413 ues the $\Delta(^{30/28}Si)_{solution}$ values are stable (within the error of analyses) and
414 remain close to the initial value of the solution of $\Delta(^{30/28}Si)_{solution} \approx 0‰$.
415 This observation remains valid even after significant precipitation of silica
416 has occurred, in particular at acidic conditions in series (a) and at neutral
417 conditions in series (b) (see Figure 1).

418 For the high-Al experimental series (c) (1 mmol/l Al), a pronounced increase
419 in $\Delta(^{30/28}Si)_{solution}$ is observed during the first 20 days, followed by a decline
420 to almost initial compositions after reaching a peak value (see Figure 5). In
421 the high-Al experiment at pH 7, the initial $\Delta(^{30/28}Si)_{solution}$ is 1.30‰, as
422 Al is removed from solution before cyclic freezing even starts (see Figure
423 2 and discussion above), which leads to simultaneous removal of Si and to
424 associated isotope fractionation. With repeated cyclic freeze-thaw, more Si is
425 removed from the solution and the $\Delta(^{30/28}Si)_{solution}$ increases with runtime
426 to a peak value of 2.72‰ after 3 days. After reaching this value the Si
427 isotope signature in the solution declines to a value of $\Delta(^{30/28}Si)_{solution}$ of
428 0.78‰ after 16 days, increases to values around 1.50‰, and finally stabilizes
429 at this level. The high-Al experiment (1 mmol/l Al) at pH 4.5 shows a similar
430 behavior, except that at this pH no initial Al precipitation occurred (Figure

5), resulting in an initial $\Delta(^{30/28}Si)_{solution}$ of 0‰. After 5 days, a peak value of $\Delta(^{30/28}Si)_{solution}$ of 2.42‰ is reached. The $\Delta(^{30/28}Si)_{solution}$ remains then stable for 11 further days. After the 16th cycle or day, the $\Delta(^{30/28}Si)_{solution}$ declines continuously to a value of -0.47‰ at 131 days.

Figure 6 shows $\Delta(^{30/28}Si)_{solution}$ vs. the fraction Si remaining in solution $f_{solution}$. The high-Al experimental series (c) (1 mmol/l Al) cannot be explained with either a simple "open-system" or "closed-system" approach (Johnson et al., 2004). Therefore, the apparent Si isotope fractionation factor $\alpha^{30/28}Si_{solid/solution}$ varied during the experimental runtime. Experimental series (a) and (b) are showing no evolution in their $\Delta(^{30/28}Si)_{solution}$ values with time despite Si removal. This implies that the apparent Si isotope fractionation factor during precipitation under these conditions is $\alpha^{30/28}Si_{solid/solution} \approx 1$.

Table 1: Freeze-thaw experiments series (a), Si concentration values and $\delta(^{29/28}Si)_{NBS28}$ and $\delta(^{30/28}Si)_{NBS28}$ values as well as 95% confidence interval (CI) for experiments with no Al.

name	pH	sampling time	Al	Si	$\delta(^{29/28}Si)$	CI	$\delta(^{30/28}Si)$	CI
		[day]	[mmol/l]	[ppm]	[‰]	[‰]	[‰]	[‰]
5_0_0_s	5.0	0	-	1.77	0.01	0.07	-0.04	0.07
5_20_0_s	5.0	20	-	1.28	-0.02	0.12	-0.05	0.07
5_40_0_s	5.0	40	-	1.22	0.01	0.04	-0.01	0.02
5_50_0_s	5.0	50	-	1.30	0.03	0.04	-0.01	0.05
5_60_0_s	5.0	60	-	1.13	0.08	0.01	0.20	0.06
5_80_0_s	5.0	80	-	0.95	0.08	0.07	0.17	0.08
5_100_0_s	5.0	100	-	0.20	-0.01	0.10	-0.10	0.08
7_0_0_s	7.0	0	-	1.75	0.00	0.06	-0.13	0.20
7_20_0_s	7.0	20	-	1.79	-0.01	0.03	-0.04	0.17
7_40_0_s	7.0	40	-	1.40	-0.08	0.05	-0.13	0.14
7_50_0_s	7.0	50	-	1.50	0.01	0.07	0.05	0.31
7_60_0_s	7.0	60	-	1.41	-0.07	0.06	-0.12	0.08
7_80_0_s	7.0	80	-	1.46	-0.05	0.07	-0.08	0.11
7_100_0_s	7.0	100	-	1.49	-0.06	0.12	-0.05	0.09

* sample names: (pH)_(day)_(Al-start-conc[mmol/l])_(solution[s]

Table 2: Freeze-thaw experiments series (b), Si concentration values and $\delta(^{29/28}Si)_{NBS28}$ and $\delta(^{30/28}Si)_{NBS28}$ values as well as 95% confidence interval (CI) for experiments with 0.1 mmol/l initial Al concentration.

name	pH	sampling time	Al	Si	$\delta(^{29/28}Si)$	CI	$\delta(^{30/28}Si)$	CI
		[day]	[mmol/l]	[ppm]	[‰]	[‰]	[‰]	[‰]
4.5_start_0.1_s	4.5	start	0.08	1.42	-0.05	0.02	-0.12	0.13
4.5_1_0.1_s	4.5	1	0.09	1.42	-0.01	0.07	0.14	0.02
4.5_2_0.1_s	4.5	2	0.09	1.42	0.00	0.24	-0.09	0.03
4.5_3_0.1_s	4.5	3	0.08	1.40	0.00	0.04	0.02	0.03
4.5_4_0.1_s	4.5	4	0.08	1.39	0.05	0.00	0.07	0.05
4.5_9_0.1_s	4.5	9	0.05	1.29	0.05	0.08	0.09	0.04
4.5_16_0.1_s	4.5	16	0.08	1.36	0.00	0.05	-0.03	0.05
4.5_32_0.1_s	4.5	32	0.10	1.35	0.01	0.04	-0.02	0.09
4.5_64_0.1_s	4.5	64	0.10	1.40	-0.05	0.13	-0.14	0.34
4.5_128_0.1_s	4.5	128	0.06	0.71	-0.12	0.13	-0.24	0.21
7_0_0.1_s	7.0	0	0.10	1.71	0.04	0.78	0.03	0.67
7_20_0.1_s	7.0	20	0.02	1.08	-0.19	0.26	-0.12	0.54
7_40_0.1_s	7.0	40	0.01	0.71	-0.27	1.14	-0.08	0.60
7_60_0.1_s	7.0	60	0.02	0.24	-0.05	1.22	-0.25	0.01
7_80_0.1_s	7.0	80	0.00	0.10	-0.18	0.88	-0.16	0.50
7_100_0.1_s	7.0	100	0.01	0.79	0.19	0.06	0.50	0.74

* sample names: (pH)_(day)_(Al-start-conc[mmol/l])_(solution[s]

Table 3: Freeze-thaw experiments series (c), Si concentration values and $\delta(^{29/28}Si)_{NBS28}$ and $\delta(^{30/28}Si)_{NBS28}$ values as well as 95% confidence interval (CI) for experiments with 1 mmol/l initial Al concentration.

name*	pH	sampling time	Al	Si	$\delta(^{29/28}Si)$	CI	$\delta(^{30/28}Si)$	CI
		[day]	[mmol/l]	[ppm]	[‰]	[‰]	[‰]	[‰]
4.5_start_1_s	4.5	start	1.02	1.59	-0.11	0.26	-0.08	0.11
4.5_1_1_s	4.5	1	0.90	1.47	0.14	0.13	0.25	0.10
4.5_5_1_s	4.5	5	0.56	0.98	1.16	0.11	2.37	0.11
4.5_8_1_s	4.5	8	0.62	1.02	1.14	0.15	2.17	0.11
4.5_16_1_s	4.5	16	0.51	0.79	1.22	0.12	2.41	0.07
4.5_34_1_s	4.5	34	0.56	0.69	0.80	0.16	1.50	0.07
4.5_64_1_s	4.5	64	0.48	0.41	0.71	0.29	1.23	0.18
4.5_131_1_s	4.5	131	0.49	0.33	-0.25	0.05	-0.47	0.09
4.5_start_1_p	4.5	start	-	-	-	-	-	-
4.5_1_1_p	4.5	1	-	-	-	-	-	-
4.5_5_1_p	4.5	5	-	-	-1.54	0.41	-3.41	0.24
4.5_8_1_p	4.5	8	-	-	-1.58	0.32	-3.06	0.17
4.5_16_1_p	4.5	16	-	-	-1.18	0.40	-2.56	0.17
4.5_34_1_p	4.5	34	-	-	-0.77	0.47	-1.48	0.21
4.5_64_1_p	4.5	64	-	-	-0.26	0.19	-0.57	0.22
4.5_131_1_p	4.5	131	-	-	0.04	0.19	0.08	0.09
7_0_1_s	7.0	0	0.00	0.72	0.65	0.04	1.28	0.04
7_1_1_s	7.0	1	0.01	0.31	0.76	0.03	1.50	0.05
7_2_1_s	7.0	2	0.00	0.11	1.33	0.02	2.57	0.06
7_3_1_s	7.0	3	0.00	0.09	1.47	0.03	2.83	0.08
7_4_1_s	7.0	4	0.02	0.29	0.21	0.02	0.41	0.04
7_9_1_s	7.0	9	0.00	0.05	0.88	0.06	1.67	0.16
7_16_1_s	7.0	16	0.00	0.05	0.51	0.05	0.88	0.04
7_32_1_s	7.0	32	0.00	0.03	0.60	0.08	1.02	0.13
7_64_1_s	7.0	64	0.00	0.02	0.86	0.43	1.53	0.25
7_128_1_s	7.0	128	-	0.01				

* sample names: (pH)_(day)_(Al-start-conc[mmol/l])_(solution[s]-or-precipitate[p]

5. Discussion

5.1. Potential removal processes

During freezing, four main processes govern the removal of Si from solution (Dietzel, 2005): (i) The solubility of Si decreases with decreasing temperature in pure Si-containing solutions (Rimstidt and Barnes, 1980). (ii) During ice formation, the total amount of liquid H_2O decreases and the remaining solution becomes supersaturated with respect to amorphous silica. (iii) Al-hydroxide can precipitate from solution as the solution gets supersaturated with respect to amorphous $Al(OH)_3$ or gibbsite. Dissolved Si can then sorb onto Al-hydroxide particles. As a result hydroxyaluminosilicates (HAS), gel- or allophane-like solids that incorporate both Si and Al can form.

The removal of Si by precipitation of amorphous silica, HAS, gel or allophane-like solids from a solution that contains monosilicic acid involves polymerization of monosilicic acid to polysilicic acid. During this so-called condensation process, the reaction of monosilicic acid molecules forms disilicic acid. Disilicic acid reacts further with monosilicic acid to form trisilicic acid and tetrasilicic acid (Iler, 1979). With ongoing oligomerization cyclic tetramers form and higher orders of polymerized silicic acid, silica colloids, gel and particles form (Greenberg and Sinclair, 1955; Iler, 1979; Tarutani, 1989). In the zero-Al experimental series (a) and the low-Al experimental series (b) the removal of Si from solution is only induced by polymerization of monosilicic acid, which leads to the formation of the solid. In contrast, the removal of Si in experimental series (c) is probably forced by the formation of Al-hydroxides with which monomeric Si can co-precipitate or onto which monosilicic acid will adsorb. As a result HAS phases might form. Precipitation of Al from

solution provides ≡Al-OH surface sites which are known to be highly attractive for $Si(OH)_4$ to form Al-O-Si bonds (see Dietzel (2002) and references therein). This process ultimately leads to the formation of crystalline silicate phases such as halloysite or kaolinite (Exley et al., 2002). Therefore the presence of Al (and other ions, see e.g. Marshall and Warakomski (1980); Marshall (1980b,a)) in the system can significantly decrease the solubility of silica (Dixit et al., 2001; Van Cappellen et al., 2002). Hence in precipitation experiments Si removal is usually accelerated by the presence of Al (Willey, 1975a,b; Wada and Kubo, 1975).

We compared the number of adsorption sites available for Si fixation in our high-Al experiments to the amount of Si removed. We therefore compare the amount of Al that is precipitated (0.05 mmol Al) to the precipitated amount of Si (1.2 mmol Si; both values for the high-Al experiment (1m mmol/l Al) pH 4.5, measured after 131 days). Assuming that only monosilicic acid is adsorbed (assumption: 1 mol Al binds 1 mol Si), the amount of Al precipitated is insufficient to fixate all Si removed from solution. We therefore suggest that the high degree of supersaturation attained already during the first freeze-thaw cycles leads to the formation of negatively charged polysilicic acid molecules (see Online Supplement A Figure A.2). These polysilicic acid molecules have a much higher affinity for Al precipitates surfaces, as shown experimentally (Dietzel and Böhme, 1997; Taylor et al., 1997). Furthermore polysilicic acid molecules form at the surface of Al-hydroxides, which provides an important mechanism to fixate Si onto Al-hydroxides (Jepson et al., 1976; Yokoyama et al., 1982; Dietzel, 2002). Therefore, the adsorption of polysilicic acid can account for the relatively large amount of Si adsorbed/precipitated

in our high-Al experiments.

5.2. Isotope fractionation associated with Si removal

Our experimental design does not allow us to determine Si removal rates and the isotopic composition under constant conditions. Parameters like temperature, Si saturation index, Si solubility and ionic strength change during freeze-thaw cycles. However, the system does evolve into a state where Si concentration and therefore the net solid formation rate is constant. To illustrate these different stages we next explore the kinetics and their change during a freeze-thaw experiment.

The kinetics of monosilicic acid removal from solution, as observed in our zero- and low-Al series (a) and (b), has been investigated over decades. A range of possible kinetic models have been derived from measurements of the time-dependent decrease of monosilicic acid in solution (see summary in Tobler et al. (2009)). Icopini et al. (2005) suggested that during the formation of di- and trisilicic acid an equilibrium is immediately attained and that further oligomerization of silicic acid is a fast process (Conrad et al., 2007). The ongoing formation from nanocolloidal silica to a solid precipitate in contrast is a slow process (Conrad et al., 2007). Given these previous findings we suggest that for the experimental series (a) and (b) the mechanisms responsible for the potentially entailing isotope fractionation (Si isotope fractionation during the formation of di-, tri and tetrasilicic acid; as no Al is involved) occur rapidly. One possible explanation for the stable Si isotopic composition of the solution despite fast reaction rates in the zero-Al and low-Al experimental series (a) and (b) is that the a net isotope fractionation between the original Si in solution, the polymerized form of silicic acid and the solid that

eventually forms is $\alpha^{30/28}Si_{solid/solution} = 1$. During reactions of tetrasilicic acids to higher polymerized silicic acid no further isotope fractionation is expected due to the high mass of these molecules (molecular mass > 120). We therefore suggest that in the absence of Al the rate at which pure Si precipitates are formed does not impact the resulting isotope fractionation.

In contrast to series (a) and (b) a strong initial Si isotope fractionation accompanies Si removal from solution in the high-Al series (c). We tested different kinetic rate laws (zeroth-order, first-order, second-order) for unidirectional precipitation only to explain the evolution of Si concentration with time. Only an irreversible second-order kinetic rate law, assuming a net rate constant, is able to fit the measured evolution of Si concentration with time assuming irreversible precipitation (see Online Supplement B). We use the Si isotope results to further evaluate this description whether the governing process of net solid formation is a unidirectional and irreversible precipitation reaction. In this case an open-system type isotope mass balance fractionation model should be applicable (Johnson et al., 2004). For the first freeze-thaw cycles such precipitation results in a reasonable fractionation factor ($\Delta(^{30/28}Si)_{solid-solution} \approx -4.3‰$, Online Supplement B). However this mass balance approach fails with ongoing experimental runtime, as unusually large Si isotope fractionation between solid and solution result for the later stages of the experiment ($\Delta(^{30/28}Si)_{solid-solution} \approx +8‰$, Online Supplement B). Such large enrichment of heavy ^{30}Si within a solid product has never been observed nor predicted by first principle equilibrium isotope fractionation calculations (Méheut et al., 2007, 2009; Méheut and Schauble, 2014; Opfergelt and Delmelle, 2012). Hence we conclude that solely unidirectional

precipitation is not a process in operation in these experiments.

We propose instead that the evolution of dissolved Si is governed by the alternation between precipitation (freezing-stage) and dissolution of the precipitated solid (thawing-stage). We propose further that net precipitation and net dissolution both follow a first-order rate law, as shown for quartz dissolution-precipitation reactions (Dove and Rimstidt (1994); see Online Supplement B). An important prerequisite of this model is that the Si fixated during freezing can dissolve rapidly during thawing. Dietzel (2005) showed that up to 95% of the fixated Si during freezing-thawing experiments is released into solution within 3 days. This release translates into rates of $\approx 1*10^{-10}$ mol*m^{-2}*sec^{-1} (assuming a surface area of hydrated amorphous silica of $\approx$1000 m^2*g^{-1}; Iler (1979)). This rate is much faster than dissolution rates for amorphous silica determined experimentally at constant temperature ($1*10^{-12}$ mol*m^{-2}*sec^{-1} at 20°C; e.g. Icenhower and Dove (2000)). The reason for such high dissolution rates observed in our experiments might be the metastability of the amorphous silica formed or its small particle size, where surface areas might be much higher than the assumed 1000 m^2*g^{-1}.

Using this framework of precipitation and dissolution reactions, results from the high-Al experimental series (c) (1 mmol/l Al) can be described as follows: (1.) The increase of $\Delta(^{30/28}Si)_{solution}$ during the first 20 days can be attributed to kinetic isotope fractionation during unidirectional attachment of Si onto Al-hydroxides (precipitation dominates over dissolution). As a result, the precipitate is strongly enriched in ^{28}Si (Oelze et al., 2014).
(2.) In the second phase of the experiment, $\Delta(^{30/28}Si)_{solution}$ values return to the initial isotopic composition (close to 0‰ for the experiment at pH 4.5

and close to 1.30‰ for the experiment pH 7). Although the dissolved Si concentrations do not change, solids have to undergo dissolution-reprecipitation cycles for their isotope composition to change.

At the end of the experiments, concentrations are at steady-state. Therefore the $\Delta(^{30/28}Si)_{solution}$ value at the end of the experiment reflects what we call here dynamic steady-state isotope fractionation. It is difficult to attribute this steady-state isotope fractionation to either equilibrium or kinetic effects, as we lack independent estimates of the equilibrium fractionation factor. Theoretical calculations predict that the phase with the higher degree of polymerization should be enriched in ^{30}Si (Ding et al., 1996; Méheut et al., 2007). Further calculations of Méheut et al. (2009), Polyakov and Mineev (2000) and Schauble (2001) show that in a covalent bonding environment heavy isotopes are favored, because they lower the zero-point energy and therefore stronger bonds are formed. Considering these previous studies we expect that at equilibrium either no isotope fractionation or preferential incorporation of heavy Si isotopes into the formed solids occurs. Therefore it seems that our experimental results are consistent with theoretical predictions of isotopic equilibrium, although the system does not reach thermodynamic or isotopic equilibrium.

5.3. Rate dependence of Si isotope fractionation

We suggest that both precipitation and dissolution reactions are accompanied by Si isotope fractionation. The change of the net precipitation and net dissolution rates through time, combined with two associated isotope fractionation factors, leads to a change in the bulk fractionation factor due

to simple mass balance effects. Figure 7 shows how the measured net solid formation rate changes along with the relative isotopic difference between solid and solution.

It is possible that a change in surface area of the solids influences the apparent fractionation factor, as it will affect the exchange flux. Unfortunately the determination of the actual surface area of the formed reactive solids is virtually impossible, as the area will be altered once the solids are removed from the ambient solution.

Regardless of this effect, we can infer that the isotopic difference between solid and solution $\Delta(^{30/28}Si)_{solid-solution}$ changes with time from a kinetically dominated regime at high net solid formation rates, where light Si isotopes are rapidly withdrawn from the solution into the solid, to a dynamic steady-state regime, where the Si concentration is nearly constant between cycles. In this regime the isotopic difference between solid and solution, compared to the kinetic regime, is very small. We show a model of this evolution in Figure 7 for the high-Al experiment at pH 4.5 (1 mmol/l Al) (see Model 3 in Online Supplement B). We model continuous precipitation and dissolution assuming two opposing first-order reactions, which are associated with respective isotope fractionation factors $\alpha^{30/28}Si_{prec}$ and $\alpha^{30/28}Si_{diss}$. We find that for the high Al experiments the most likely case is one where the major part of the formed solid redissolves and exchanges with the solution at each cycle. The best fit values of the developed isotope mass balance model (see Figure B.2 in the Online Supplement B) yields isotope fractionation factors for precipitation and dissolution of $\alpha^{30/28}Si_{prec}$ =0.9953 ($10^3 ln\alpha_{prec}$ = -4.7‰) and $\alpha^{30/28}Si_{diss}$ =0.9947 ($10^3 ln\alpha_{diss}$ = -5.3‰) for the experiment at

pH 4.5 and $\alpha^{30/28}Si_{prec}$ =0.9989 to 0.9991 ($10^3 ln\alpha_{prec}$ = -1.1 to -0.9‰) and $\alpha^{30/28}Si_{diss}$ =0.9992 to 0.9994 ($10^3 ln\alpha_{diss}$ = -0.8 to -0.6‰) for the experiment at pH 7, respectively.

The initial kinetic isotope fractionation factor, where net-precipitation dominates, is likely governed by chemisorption processes. These values are similar to the fractionation factors found in the Oelze et al. (2014) adsorption experiments (-1.8‰ to -3‰, depending on Si concentration). This initial Si isotope fractionation factor, probably reaches the kinetic limit of Si isotope fractionation (Nielsen et al., 2012; Druhan et al., 2013). Therefore it might represent the absolute maximum kinetic Si isotope fractionation factor for Si during precipitation. Above this kinetic limit an increase of the precipitation rate is not accompanied by a further increase in the isotope fractionation factor (see Figure 8 in Nielsen et al. (2012)).

In the zero-Al and low-Al experimental series (a) and (b), the initial phase involving kinetic isotope fractionation is not encountered, and the system evolves with an apparent isotope fractionation factor of $\alpha^{30/28}Si_{solid/solution}$ =1 ($10^3 ln\alpha_{solid/solution}$ = 0‰). In all high-Al experiments, towards the end the Si isotope fractionation at steady-state is also close to $\alpha^{30/28}Si_{solid/solution}$ =1 ($10^3 ln\alpha_{solid/solution}$ = 0‰).

6. Summary and implications

We have demonstrated that, during cyclic freeze-thaw of dissolved Si-containing solutions, Si is removed from the solution. In the absence of appreciable amounts of Al this removal is not accompanied by the fractionation of Si isotopes. The formation of di-, tri- and tetrasilicic acid apparently proceeds with a Si isotope fractionation factor $\alpha^{30/28}Si_{solid/solution}$ =1 ($10^3 ln\alpha_{solid/solution}$ = 0‰). With subsequent oligomerization and formation of almost pure Si solids no further Si isotope fractionation is expected due to the high molecular masses involved. To conclude, the precipitation of pure Si solids does not lead to any Si isotope fractionation.

In contrast if Al is present in these solutions at high concentrations (i.e. here 1 mmol/l), Si removal is faster and accompanied by strong Si isotope fractionation favoring the light isotopes in the solids. For these high Al experiments we calculate a fractionation factor of up to $\alpha^{30/28}Si_{solid/solution}$ =0.9950 ($10^3 ln\alpha_{solid/solution}$ = -5‰) for the first 20 days of the experiment . This strong initial isotope fractionation occurs during adsorption or binding of Si onto Al-hydroxide (Oelze et al., 2014). With ongoing runtime the early formed precipitates are reorganized wholesale, such that $\alpha^{30/28}Si_{solid/solution}$ =1 ($10^3 ln\alpha_{solid/solution}$ = 0‰). Hence after attaining steady-state conditions no Si isotope fractionation during solid reorganization occurs. It is likely that the zero fractionation factor observed in the final phase of the high-Al experimental series (c) and in the low- and zero-Al experiments represents the equilibrium isotope fractionation factor of silica precipitation.

Regarding silicate weathering this study implies that where secondary precipitates (such as metastable silica-containing solids) are formed, kinetic isotope

effects will be dominating. Secondary minerals formed with high Al/Si ratios, will be enriched in ^{28}Si (see Savage et al. (2013); Cornelis et al. (2014)). This conclusion is supported by the observation that Si measured in river water is enriched in ^{30}Si over the host rock (e.g. Ziegler et al. (2005b); Georg et al. (2006a); Opfergelt et al. (2009); Bern et al. (2010); Steinhoefel et al. (2011), while secondary soil minerals are mostly depleted in ^{30}Si. Moreover, this study suggests that slowly re-organization or recrystallization of these solids is likely accompanied by negligible Si isotope fractionation.

During silicification of sediments a variety of isotope fractionation factors are likely to be in operation, depending on individual environmental conditions. If solutions are supersaturated with respect to opal-A or opal-CT and free of "impurities" (no Al or other carrier phases present) they will probably precipitate with an Si isotope fractionation factor of $\alpha^{30/28}Si_{solid/solution}$ =1 ($10^3 ln\alpha^{30/28}Si_{solid/solution}$ of 0‰). In contrast, the presence of Al in the system increases the precipitation rate (Wada and Kubo, 1975; Willey, 1975b) and therefore Si isotopes will fractionate according to the Al/Si ratio. The difference between the rapidly precipitating Al-containing phase compared to the slowly precipitating Al-free phase is then reflected in the Si isotope composition of these two phases, with the higher enrichment of ^{28}Si in the Al-containing phase.

The inferred absence of any $\alpha^{30/28}Si_{solid/solution}$ >1 ($10^3 ln\alpha^{30/28}Si_{solid/solution}$ > 0‰) between solid and solution implies that in the geologic record Si isotope ratios exceeding that of their source materials are likely to be a mass balance effect stemming from fast precipitation of solids enriched in light Si isotope.

To conclude, the enrichment of light Si isotopes in geologic low-temperature

processes is related to fast precipitation of secondary solids as induced by co-precipitation of Al phases or another carrier phase (e.g. Fe(III)). In contrast no Si isotope fractionation can be expected between solid and solution during slow precipitation under equilibrium conditions.

7. Acknowledgments

We are grateful to Kate Maher, Jenny Druhan, Joey Nelson and two anonymous reviewers for their thorough comments on this paper. We thank Michael Tatzel for continuous fruitful discussions about freeze-thaw and proof reading and further Jan Schuessler for his continuous laboratory support. We also thank M. Boettcher for the editorial handling of this manuscript. This work is dedicated to Carola Ocholt.

8. References

Abraham, K., Cardinal, D., Hofmann, A., Foley, S. F., Harris, C., Barth, M. G., Andre, L., Jan. 2011. Coupled silicon–oxygen isotope fractionation traces Archaean silicification. Earth and Planetary Science Letters 301 (1-2), 222–230.

Anderson, D. M., 1981. Some thermodynamic relationships governing the behavior of permafrost and patterned ground. Tech. Rep. NASA TM-84211.

Anderson, D. M., Tice, A. R., 1973. The Unfrozen Interfacial Phase in Frozen Soil Water Systems. In: Physical Aspects of Soil Water and Salts in Ecosystems. Springer Berlin Heidelberg, Berlin, Heidelberg, pp. 107–124.

Andre, L., Cardinal, D., Alleman, L. Y., Moorbath, S., 2006. Silicon isotopes in 3.8 Ga West Greenland rocks as clues to the Eoarchaean supracrustal Si cycle. Earth and Planetary Science Letters 245 (1-2), 162–173.

Armytage, R. M. G., Georg, R. B., Savage, P. S., Williams, H. M., Halliday, A. N., 2011. Silicon isotopes in meteorites and planetary core formation. Geochimica et Cosmochimica Acta 75 (13), 3662–3676.

Basile-Doelsch, I., Meunier, J. D., Parron, C., 2005. Another continental pool in the terrestrial silicon cycle. Nature 433 (7024), 399–402.

Bern, C. R., Brzezinski, M. A., Beucher, C., Ziegler, K., Chadwick, O. A., 2010. Weathering, dust, and biocycling effects on soil silicon isotope ratios. Geochimica et Cosmochimica Acta 74 (3), 876–889.

Carroll, S., Mroczek, E., Alai, M., Ebert, M., Jan. 1998. Amorphous silica precipitation (60 to 120°C): Comparison of laboratory and field rates. Geochimica et Cosmochimica Acta 62 (8), 1379–1396.

Chakrabarti, R., Knoll, A. H., Jacobsen, S. B., Fischer, W. W., 2012. Si isotope variability in Proterozoic cherts. Geochimica et Cosmochimica Acta 91, 187–201.

Chen, Y., Jiang, S., Ling, H., Yang, J., Wan, D., Jul. 2007. Isotopic compositions of small shelly fossil Anabarites from Lower Cambrian in Yangtze Platform of South China: Implications for palaeocean temperature. Progress in Natural Science 17 (10), 1185–1191.

Chmeleff, J., Horn, I., Steinhoefel, G., von Blanckenburg, F., 2008. In situ determination of precise stable Si isotope ratios by UV-femtosecond laser

731 ablation high-resolution multi-collector ICP-MS. Chemical Geology 249 (1-
732 2), 155–166.

733 Cole, D. R., Ohmoto, H., Lasaga, A. C., Oct. 1983. Isotopic exchange in
734 mineral-fluid systems. I. Theoretical evaluation of oxygen isotopic exchange
735 accompanying surface reactions and diffusion. Geochimica et Cosmochim-
736 ica Acta 47 (10), 1681–1693.

737 Conrad, C. F., Icopini, G. A., Yasuhara, H., Bandstra, J. Z., Brantley, S. L.,
738 Heaney, P. J., Feb. 2007. Modeling the kinetics of silica nanocolloid forma-
739 tion and precipitation in geologically relevant aqueous solutions. Geochim-
740 ica et Cosmochimica Acta 71 (3), 531–542.

741 Coplen, T., Böhlke, J., de Bièvre, P., Ding, T., Holden, N., Hopple, J.,
742 Krouse, H., Lamberty, A., Peiser, H., Revesz, K., 2002. Isotope-abundance
743 variations of selected elements:(IUPAC technical report). Pure and applied
744 chemistry 74 (10), 1987–2017.

745 Coplen, T. B., 2011. Guidelines and recommended terms for expression of
746 stable-isotope-ratio and gas-ratio measurement results. Rapid Communi-
747 cations in Mass Spectrometry 25 (17), 2538–2560.

748 Cornelis, J.-T., Weis, D., Lavkulich, L., Vermeire, M.-L., Delvaux, B., Bar-
749 ling, J., 2014. Silicon isotopes record dissolution and re-precipitation of
750 pedogenic clay minerals in a podzolic soil chronosequence. Geoderma 235-
751 236 (C), 19–29.

752 Criss, R. E., Gregory, R. T., Taylor Jr, H. P., 1987. Kinetic theory of oxygen

isotopic exchange between minerals and water. Geochimica et Cosmochimica Acta 51 (5), 1099–1108.

de La Rocha, C. L., Brzezinski, M. A., DeNiro, M. J., Jul. 2000. A first look at the distribution of the stable isotopes of silicon in natural waters. Geochimica et Cosmochimica Acta 64 (14), 2467–2477.

Delstanche, S., Opfergelt, S., Cardinal, D., Elsass, F., Elsass, F., André, L., Delvaux, B., 2009. Silicon isotopic fractionation during adsorption of aqueous monosilicic acid onto iron oxide. Geochimica et Cosmochimica Acta 73 (4), 923–934.

DePaolo, D. J., 2011. Surface kinetic model for isotopic and trace element fractionation during precipitation of calcite from aqueous solutions. Geochimica et Cosmochimica Acta 75 (4), 1039–1056.

Dickinson, W. W., Grapes, R. H., Sep. 1997. Authigenic chabazite and implications for weathering in Sirius Group diamictite, Table Mountain, dry valleys, Antarctica. Journal of Sedimentary Research 67 (5), 815–820.

Dietzel, M., Jan. 1993. Depolymerisation von hochpolymerer Kieselsäure in wässriger Lösung. Ph.D. thesis, University Göttingen, Göttingen.

Dietzel, M., Jan. 2000. Dissolution of silicates and the stability of polysilicic acid. Geochimica et Cosmochimica Acta 64 (19), 3275–3281.

Dietzel, M., 2002. Interaction of polysilicic and monosilicic acid with mineral surfaces. In: Stober, I., Bucher, K. (Eds.), Water Science and Technology Library. Springer Netherlands, pp. 207–235.

775 Dietzel, M., Jan. 2005. Impact of cyclic freezing on precipitation of silica
776 in Me-SiO2-H2O systems and geochemical implications for cryosoils and
777 -sediments. Chemical Geology 216 (11), 79–88.

778 Dietzel, M., Böhme, G., 1997. Adsorption and Stability of Polymeric Silica
779 — Adsorption und Stabilität von polymerer Kieselsäure. Chemie der Erde
780 - Geochemistry 57 (2-3), 189–203.

781 Ding, T., Jiang, S., Wan, D., Li, Y., Li, J., Song, H., Liu, Z., Yao, X.,
782 1996. Silicon Isotope Geochemistry. Geological Publishing House, Beijing,
783 China.

784 Dixit, S., Van Cappellen, P., van Bennekom, A. J., Mar. 2001. Processes
785 controlling solubility of biogenic silica and pore water build-up of silicic
786 acid in marine sediments. Marine Chemistry 73 (3-4), 333–352.

787 Douthitt, C. B., 1982. The geochemistry of the stable isotopes of silicon.
788 Geochimica et Cosmochimica Acta 46 (8), 1449–1458.

789 Dove, P. M., Han, N., Wallace, A. F., De Yoreo, J. J., 2008. Kinetics of
790 amorphous silica dissolution and the paradox of the silica polymorphs.
791 Proceedings of the National Academy of Sciences 105 (29), 9903–9908.

792 Dove, P. M., Rimstidt, J. D., 1994. Silica-water interactions. Reviews in
793 Mineralogy and Geochemistry 29 (1), 259–308.

794 Druhan, J. L., Steefel, C. I., Williams, K. H., DePaolo, D. J., Oct. 2013.
795 Calcium isotope fractionation in groundwater: Molecular scale processes
796 influencing field scale behavior. Geochimica et Cosmochimica Acta 119,
797 93–116.

798 Exley, C., Schneider, C., Doucet, F., 2002. The reaction of aluminium with
799 silicic acid in acidic solution: an important mechanism in controlling the
800 biological availability of aluminium? Coordination Chemistry Reviews
801 228 (2), 127–135.

802 Fitoussi, C., Bourdon, B., Kleine, T., Oberli, F., Reynolds, B. C., Jan. 2009.
803 Si isotope systematics of meteorites and terrestrial peridotites: implica-
804 tions for Mg/Si fractionation in the solar nebula and for Si in the Earth's
805 core. Earth and Planetary Science Letters 287 (1-2), 77–85.

806 Geilert, S., Vroon, P. Z., Roerdink, D. L., van CAPPELLEN, P., van Bergen,
807 M. J., 2014. Silicon isotope fractionation during abiotic silica precipitation
808 at low temperatures: Inferences from flow-through experiments. Geochim-
809 ica et Cosmochimica Acta 142 (1), 95–114.

810 Georg, R. B., Halliday, A. N., Schauble, E. A., Reynolds, B. C., Jan. 2007.
811 Silicon in the Earth's core. Nature 447 (7148), 1102–1106.

812 Georg, R. B., Reynolds, B. C., Frank, M., Halliday, A. N., 2006a. Mechanisms
813 controlling the silicon isotopic compositions of river waters. Earth and
814 Planetary Science Letters 249, 290–306.

815 Georg, R. B., Reynolds, B. C., Frank, M., Halliday, A. N., Jan. 2006b. New
816 sample preparation techniques for the determination of Si isotopic compo-
817 sitions using MC-ICPMS. Chemical Geology 235 (1-2), 95–104.

818 Georg, R. B., Zhu, C., Reynolds, B. C., Halliday, A. N., Apr. 2009. Stable
819 silicon isotopes of groundwater, feldspars, and clay coatings in the Navajo

820 Sandstone aquifer, Black Mesa, Arizona, USA. Geochimica et Cosmochim-
821 ica Acta 73 (8), 2229–2241.

822 Gislason, S. R., Oelkers, E., Jan. 2003. Mechanism, rates, and consequences
823 of basaltic glass dissolution: II. An experimental study of the dissolution
824 rates of basaltic glass as a function of pH and temperature. Geochimica et
825 Cosmochimica Acta 67 (20), 3817–3832.

826 Greenberg, S. A., Sinclair, D., May 1955. The polymerization of silicic acid.
827 Journal of Physical Chemistry 59 (5), 435–440.

828 Gunnarsson, I., Arnorsson, S., Jul. 2000. Amorphous silica solubility and the
829 thermodynamic properties of $H_4SiO^\circ_4$ the range of 0° to 350°C at P_{sat}.
830 Geochimica et Cosmochimica Acta 64 (13), 2295–2307.

831 Hingston, F., Raupach, M., 1967. The reaction between monosilicic acid and
832 aluminium hydroxide. I. Kinetics of adsorption of silicic acid by aluminium
833 hydroxide. Australian Journal of Soil Research 5 (2), 295–309.

834 Hofmann, A. E., Bourg, I. C., DePaolo, D. J., 2012. Ion desolvation as a
835 mechanism for kinetic isotope fractionation in aqueous systems. Proceed-
836 ings of the National Academy of Sciences 109 (46), 18689–18694.

837 Icenhower, J., Dove, P. M., Jan. 2000. The dissolution kinetics of amor-
838 phous silica into sodium chloride solutions: Effects of temperature and
839 ionic strength. Geochimica et Cosmochimica Acta 64 (24), 4193–4203.

840 Icopini, G., Brantley, S. L., Heaney, P., Jan. 2005. Kinetics of silica oligomer-
841 ization and nanocolloid formation as a function of pH and ionic strength
842 at 25°C. Geochimica et Cosmochimica Acta 69 (2), 293–303.

Iler, R. K., 1979. The chemistry of silica: solubility, polymerization, colloid and surface properties, and biochemistry. John Wiley & Sons, Inc., New York.

Jepson, W., Jeffs, D., Ferris, A., 1976. The adsorption of silica on gibbsite and its relevance to the kaolinite surface. Journal of Colloid and Interface Science 55 (2), 454–461.

Johnson, C. M., Beard, B. L., Albarede, F., Jan. 2004. Overview and general concepts. Reviews in Mineralogy and Geochemistry 55, 1–24.

Johnson, C. M., Skulan, J., Beard, B., Sun, H., Nealson, K., Braterman, P., 2002. Isotopic fractionation between Fe(III) and Fe(II) in aqueous solutions. Earth and Planetary Science Letters 195, 141–153.

Li, W., Beard, B. L., Johnson, C. M., 2011. Exchange and fractionation of Mg isotopes between epsomite and saturated $MgSO_4$ solution. Geochimica et Cosmochimica Acta 75 (7), 1814–1828.

Li, Y., Ding, T., Wan, D., 1995. Experimental study of silicon isotope dynamic fractionation and its application in geology. Chinese Journal of Geochemistry 14 (3), 212–219.

Marshall, W. L., Jul. 1980a. Amorphous silica solubilities—I. Behavior in aqueous sodium nitrate solutions; 25–300°C, 0–6 molal. Geochimica et Cosmochimica Acta 44 (7), 907–913.

Marshall, W. L., Jul. 1980b. Amorphous silica solubilities—III. Activity coefficient relations and predictions of solubility behavior in salt solutions, 0–350°C. Geochimica et Cosmochimica Acta 44 (7), 925–931.

866 Marshall, W. L., Warakomski, J. M., Jul. 1980. Amorphous silica solubil-
867 ities—II. Effect of aqueous salt solutions at 25°C. Geochimica et Cos-
868 mochimica Acta 44 (7), 915–924.

869 Méheut, M., Lazzeri, M., Balan, E., Mauri, F., 2007. Equilibrium isotopic
870 fractionation in the kaolinite, quartz, water system: Prediction from first-
871 principles density-functional theory. Geochimica et Cosmochimica Acta
872 71 (13), 3170–3181.

873 Méheut, M., Lazzeri, M., Balan, E., Mauri, F., Jan. 2009. Structural con-
874 trol over equilibrium silicon and oxygen isotopic fractionation: A first-
875 principles density-functional theory study. Chemical Geology 258 (1-2),
876 28–37.

877 Méheut, M., Schauble, E. A., 2014. Silicon isotope fractionation in silicate
878 minerals: Insights from first-principles models of phyllosilicates, albite and
879 pyrope. Geochimica et Cosmochimica Acta 134, 137–154.

880 Nielsen, L. C., DePaolo, D. J., de Yoreo, J. J., 2012. Self-consistent ion-by-ion
881 growth model for kinetic isotopic fractionation during calcite precipitation.
882 Geochimica et Cosmochimica Acta 86, 166–181.

883 Oelze, M., von Blanckenburg, F., Hoellen, D., Dietzel, M., Bouchez, J., Jul.
884 2014. Si stable isotope fractionation during adsorption and the competition
885 between kinetic and equilibrium isotope fractionation: Implications for
886 weathering systems. Chemical Geology 380, 161–171.

887 Opfergelt, S., de Bournonville, G., Cardinal, D., André, L., Delstanche,
888 S., Delvaux, B., 2009. Impact of soil weathering degree on silicon iso-

889 topic fractionation during adsorption onto iron oxides in basaltic ash soils,
890 Cameroon. Geochimica et Cosmochimica Acta 73 (24), 7226–7240.

891 Opfergelt, S., Delmelle, P., Nov. 2012. Silicon isotopes and continental weath-
892 ering processes: Assessing controls on Si transfer to the ocean. Comptes
893 rendus - Geoscience 344 (11-12), 723–738.

894 Parkhurst, D. L., Appelo, C. A. J., 1999. User‘s guide to PHREEQC (Version
895 2) : a computer program for speciation, batch-reaction, one-dimensional
896 transport, and inverse geochemical calculations. US Geological Survey
897 Water-Resources Investigations Report 99-4259, 312.

898 Polyakov, V. B., Mineev, S. D., Mar. 2000. The use of Mössbauer spec-
899 troscopy in stable isotope geochemistry. Geochimica et Cosmochimica Acta
900 64 (5), 849–865.

901 Renders, P. J. N., Gammons, C. H., Barnes, H. L., Jan. 1995. Precipitation
902 and dissolution rate constants for cristobalite from 150 to 300°C. Geochim-
903 ica et Cosmochimica Acta 59 (1), 77–85.

904 Reynolds, B. C., Aggarwal, J., André, L., Baxter, D., Beucher, C., Brzezinski,
905 M. A., Engström, E., Georg, R. B., Land, M., Leng, M. J., Opfergelt, S.,
906 Rodushkin, I., Sloane, H. J., van den Boorn, S. H. J. M., Vroon, P. Z., Car-
907 dinal, D., May 2007. An inter-laboratory comparison of Si isotope reference
908 materials. Journal of Analytical Atomic Spectrometry 22 (5), 561–568.

909 Richter, F. M., Mendybaev, R., Christensen, J., Hutcheon, I., Williams, R.,
910 Sturchio, N., Beloso, A., 2006. Kinetic isotopic fractionation during diffu-

911 sion of ionic species in water. Geochimica et Cosmochimica Acta 70 (2),
912 277–289.

913 Rimstidt, J. D., Barnes, H. L., Nov. 1980. The kinetics of silica-water reac-
914 tions. Geochimica et Cosmochimica Acta 44 (11), 1683–1699.

915 Robert, F., Chaussidon, M., 2006. A palaeotemperature curve for the Pre-
916 cambrian oceans based on silicon isotopes in cherts. Nature 443 (7114),
917 969–972.

918 Savage, P. S., Georg, R. B., Armytage, R. M. G., Williams, H. M., Halliday,
919 A. N., Jan. 2010. Silicon isotope homogeneity in the mantle. Earth and
920 Planetary Science Letters 295 (1-2), 139–146.

921 Savage, P. S., Georg, R. B., Williams, H. M., Halliday, A. N., May 2013. The
922 silicon isotope composition of the upper continental crust. Geochimica et
923 Cosmochimica Acta 109, 384–399.

924 Schauble, E., Aug. 2001. Theoretical estimates of equilibrium Fe-isotope
925 fractionations from vibrational spectroscopy. Geochimica et Cosmochimica
926 Acta 65 (15), 2487–2497.

927 Schuessler, J. A., Schoenberg, R., Behrens, H., von Blanckenburg, F., Jan.
928 2007. The experimental calibration of the iron isotope fractionation fac-
929 tor between pyrrhotite and peralkaline rhyolitic melt. Geochimica et Cos-
930 mochimica Acta 71 (2), 417–433.

931 Schwertmann, U., Fischer, W. R., 1982. PH-Verteilung und Pufferung von
932 Böden. Zeitschrift für Pflanzenernährung und Bodenkunde 145 (2), 221–
933 223.

Steefel, C. I., Van Cappellen, P., Oct. 1990. A new kinetic approach to modeling water-rock interaction: The role of nucleation, precursors, and Ostwald ripening. Geochimica et Cosmochimica Acta 54 (10), 2657–2677.

Steinhoefel, G., Breuer, J., von Blanckenburg, F., Horn, I., Kaczorek, D., Sommer, M., 2011. Micrometer silicon isotope diagnostics of soils by UV femtosecond laser ablation. Chemical Geology 286 (3-4), 280–289.

Steinhoefel, G., Horn, I., von Blanckenburg, F., Jan. 2009. Micro-scale tracing of Fe and Si isotope signatures in banded iron formation using femtosecond laser ablation. Geochimica et Cosmochimica Acta 73 (18), 5343–5360.

Steinhoefel, G., von Blanckenburg, F., Horn, I., Konhauser, K. O., Beukes, N. J., Gutzmer, J., 2010. Deciphering formation processes of banded iron formations from the Transvaal and the Hamersley successions by combined Si and Fe isotope analysis using UV femtosecond laser ablation. Geochimica et Cosmochimica Acta 74 (9), 2677–2696.

Tang, J., Dietzel, M., Böhm, F., Köhler, S. J., Eisenhauer, A., Aug. 2008. Sr^{2+}/Ca^{2+} and $^{44}Ca/^{40}Ca$ fractionation during inorganic calcite formation: II. Ca isotopes. Geochimica et Cosmochimica Acta 72 (15), 3733–3745.

Tarutani, T., 1989. Polymerization of Silicic Acid A Review. Analytical Sciences 5 (3), 245–253.

Taylor, P. D., Jugdaohsingh, R., Powell, J. J., Sep. 1997. Soluble Silica with High Affinity for Aluminum under Physiological and Natural Conditions. Journal of the American Chemical Society 119 (38), 8852–8856.

Tedrow, J. C. F., 1966. Polar Desert Soils. Soil Science Society of America Journal 30 (3), 381.

Tobler, D. J., Shaw, S., Benning, L. G., 2009. Quantification of initial steps of nucleation and growth of silica nanoparticles: An in-situ SAXS and DLS study. Geochimica et Cosmochimica Acta 73 (18), 5377–5393.

Urey, H. C., 1947. The thermodynamic properties of isotopic substances. . Journal of the Chemical Society, 562–581.

Van Cappellen, P., Dixit, S., van Beusekom, J., 2002. Biogenic silica dissolution in the oceans: Reconciling experimental and field-based dissolution rates. Global Biogeochemical Cycles 16 (4), 23–1–23–10.

van den Boorn, S. H. J. M., van Bergen, M. J., Vroon, P. Z., de Vries, S. T., Nijman, W., Jan. 2010. Silicon isotope and trace element constraints on the origin of similar to 3.5 Ga cherts: Implications for Early Archaean marine environments. Geochimica et Cosmochimica Acta 74 (3), 1077–1103.

Wada, K., Kubo, H., 1975. Precipitation of amorphous aluminosilicates from solutions containing monomeric silica and aluminium ions. Journal of Soil Science 26 (2), 100–111.

Welch, S., Beard, B., Johnson, C. M., Braterman, P., 2003. Kinetic and equilibrium Fe isotope fractionation between aqueous Fe(II) and Fe(III). Geochimica et Cosmochimica Acta 67 (22), 4231–4250.

Willey, J., Sep. 1975a. Silica-alumina interactions in seawater. Marine Chemistry 3 (3), 241–251.

978 Willey, J. D., Sep. 1975b. Reactions which remove dissolved alumina from
979 seawater. Marine Chemistry 3 (3), 227–240.

980 Yokoyama, T., Nakamura, O., Tarutani, T., 1982. Polymerization of silicic
981 acid adsorbed on aluminium hydroxide. Bulletin of the Chemical Society
982 of Japan 55 (4), 975–978.

983 Zambardi, T., Poitrasson, F., 2011. Precise Determination of Silicon Isotopes
984 in Silicate Rock Reference Materials by MC-ICP-MS. Geostandards and
985 Geoanalytical Research 35 (1), 89–99.

986 Ziegler, K., Chadwick, O. A., Brzezinski, M. A., Kelly, E., Oct. 2005a. Nat-
987 ural variations of delta Si-30 ratios during progressive basalt weathering,
988 Hawaiian Islands. Geochimica et Cosmochimica Acta 69 (19), 4597–4610.

989 Ziegler, K., Chadwick, O. A., White, A. F., Brzezinski, M. A., Jan. 2005b.
990 (DSi)-Si-30 systematics in a granitic saprolite, Puerto Rico. Geology
991 33 (10), 817–820.

9. Figures

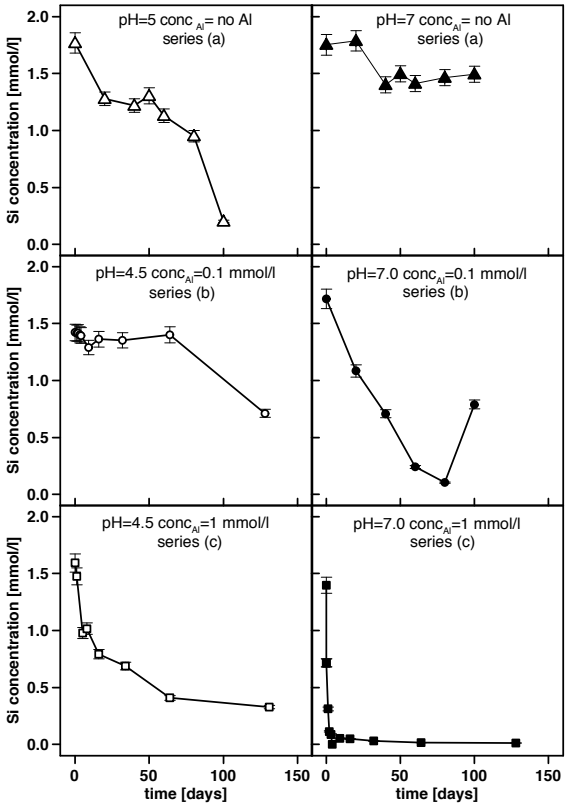

Figure 1: Evolution of Si concentration in solutions during freeze-thaw experiments. Open symbols depict experiments at pH 4.5 or pH 5 and solid symbols those at pH 7. Triangles represent zero-Al experiments, circles represent low-Al experiments (0.1 mmol/l Al) and squares high-Al experiments (1 mmol/l Al), respectively (an error of 5% was estimated for concentration measurements)

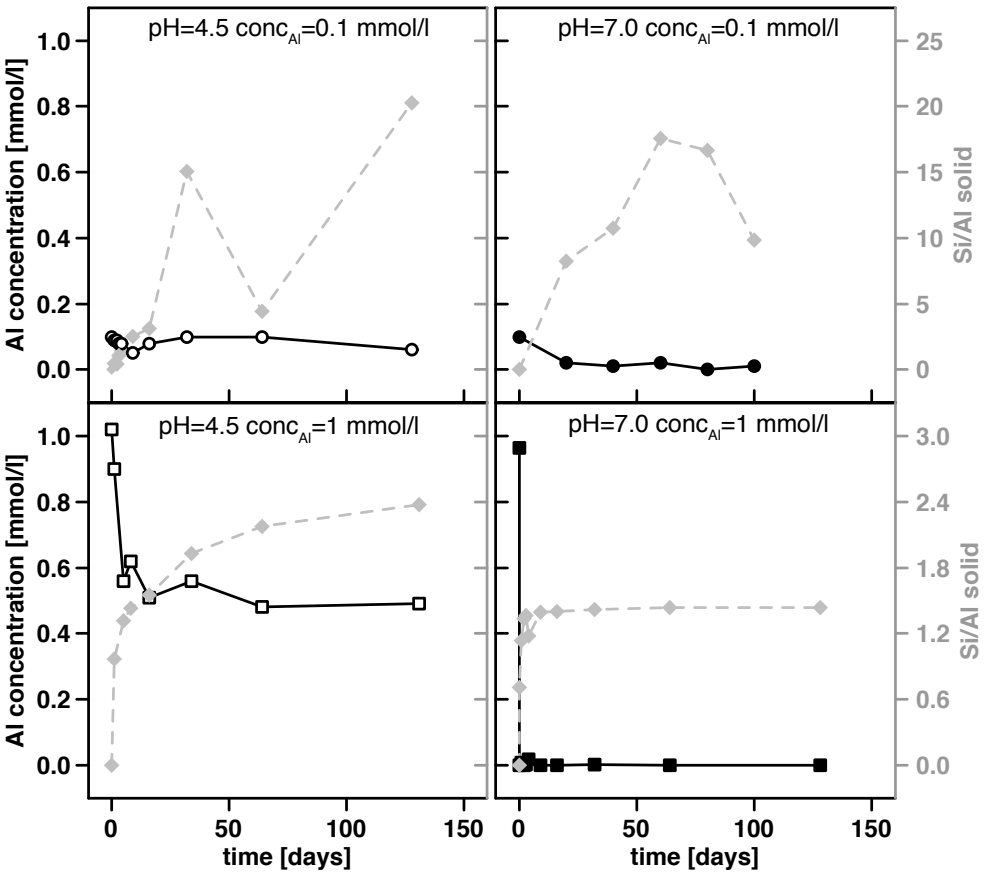

Figure 2: Evolution of Al concentration in solutions (left axis; open and solid black symbols) and evolution of Si/Al_{solid} ratios (right axis; grey symbols) in solids. Open symbols depict experiments at pH 4.5 and solid symbols those at pH 7. Circles represent low-Al experiments (0.1 mmol/l Al) and squares high-Al experiments (1 mmol/l Al), respectively (an error of 5% was estimated for concentration measurements).

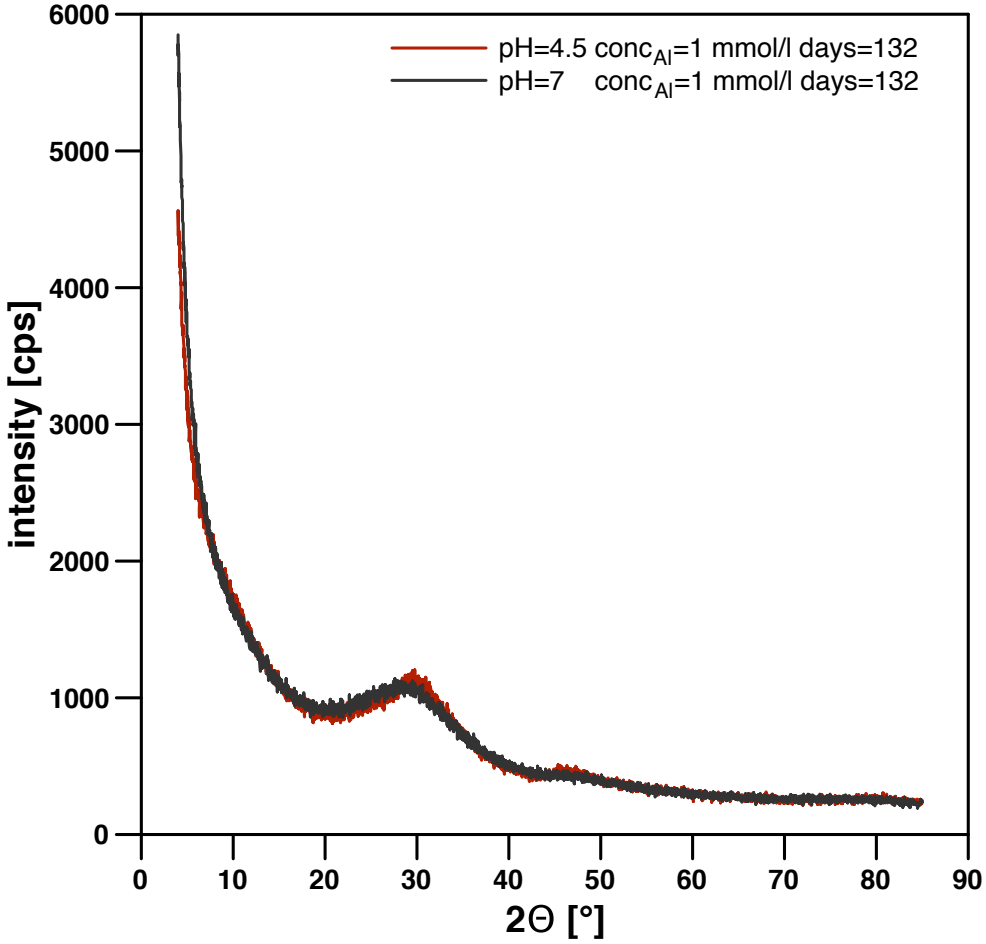

Figure 3: XRD patterns (Co-Kα) of the precipitated solid after 132 days in the high-Al experiment at pH=4.5 and pH=7. No sharp peaks can be identified and only a broad amorphous pattern is observed.

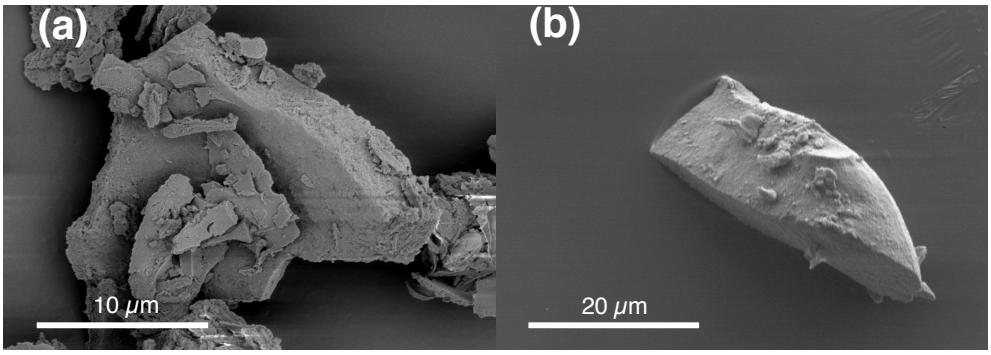

Figure 4: SEM images of precipitates (a) low-Al experiment (0.1 mmol/l Al) at pH 7, after 60 days/freeze-thaw cycles; (b) high-Al experiment (1 mmol/l Al) at pH 7, after 1 day/freeze-thaw cycles

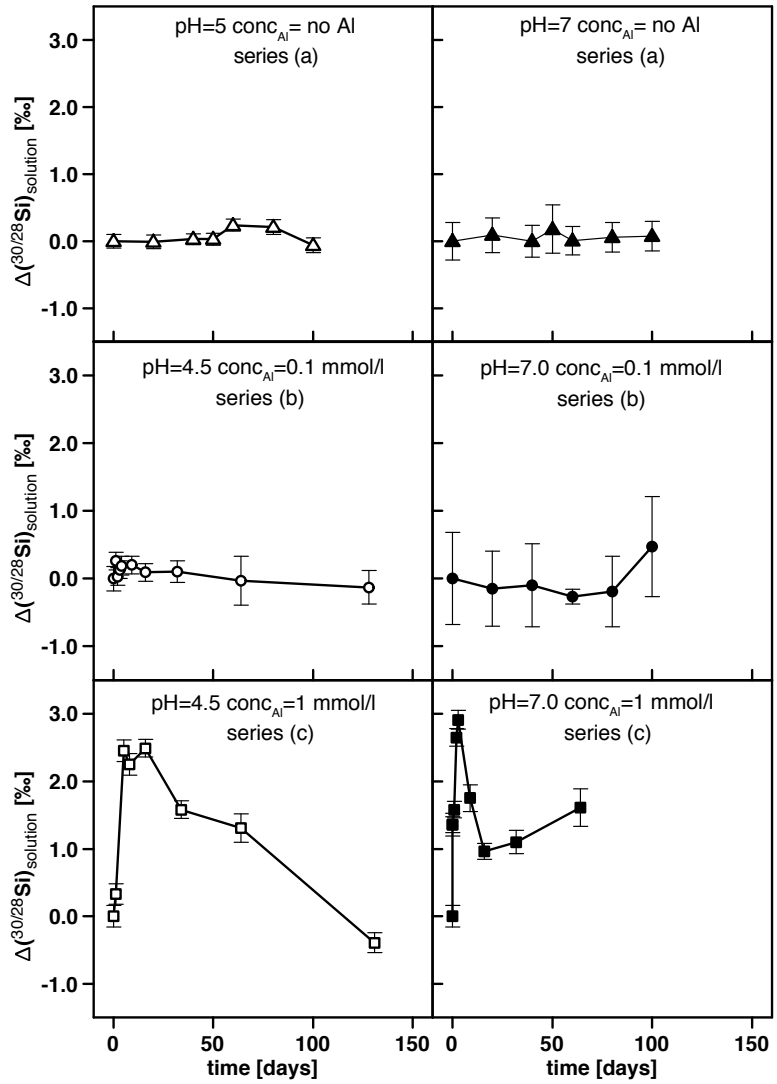

Figure 5: $\Delta(^{30/28}Si)_{solution} = \delta(^{30/28}Si)_{solution(t)} - \delta(^{30/28}Si)_{solution(initial)}$ during freeze-thaw experiments. Open symbols depict experiments at pH 4.5 or pH 5 and solid symbols those at pH 7. Triangles represent zero-Al experiments, circles represent low-Al experiments (0.1 mmol/l Al) and squares high-Al experiments (1 mmol/l Al), respectively.

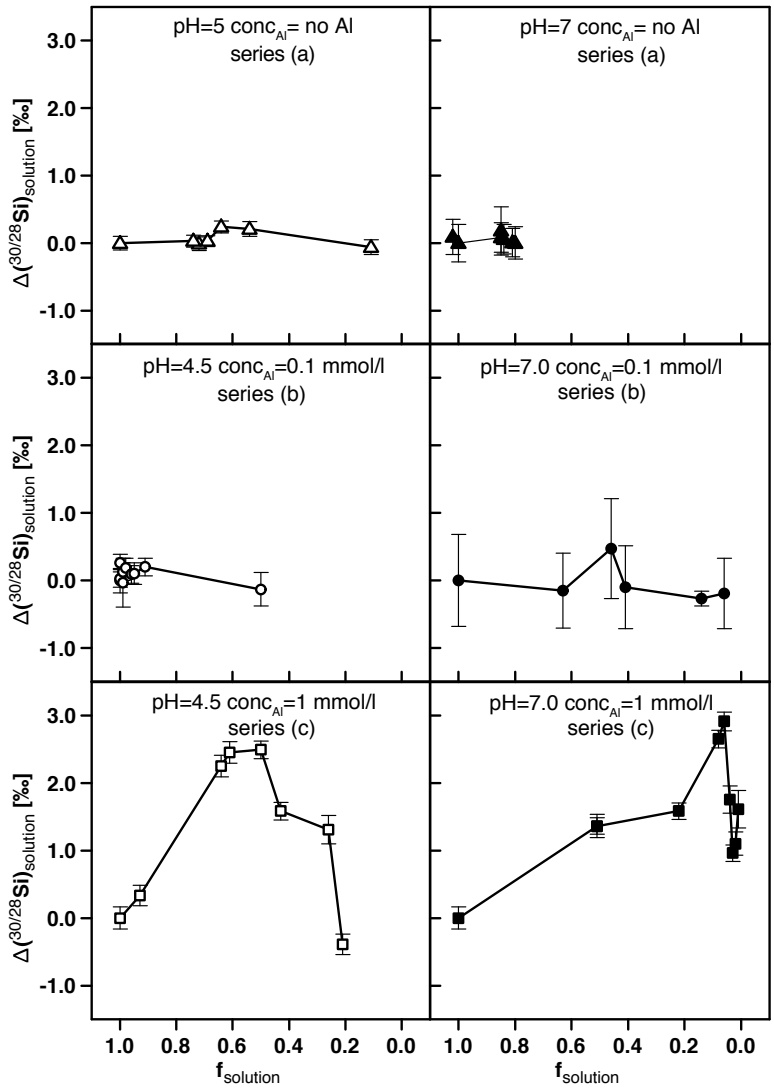

Figure 6: $\Delta(^{30/28}Si)_{solution} = \delta(^{30/28}Si)_{solution(t)} - \delta(^{30/28}Si)_{solution(initial)}$ vs. fraction Si remaining in solution ($f_{solution}$). Open symbols depict experiments at pH 4.5 or pH 5 and solid symbols those at pH 7. Triangles represent zero-Al experiments, circles represent low-Al experiments (0.1 mmol/l Al) and squares high-Al experiments (1 mmol/l Al), respectively.

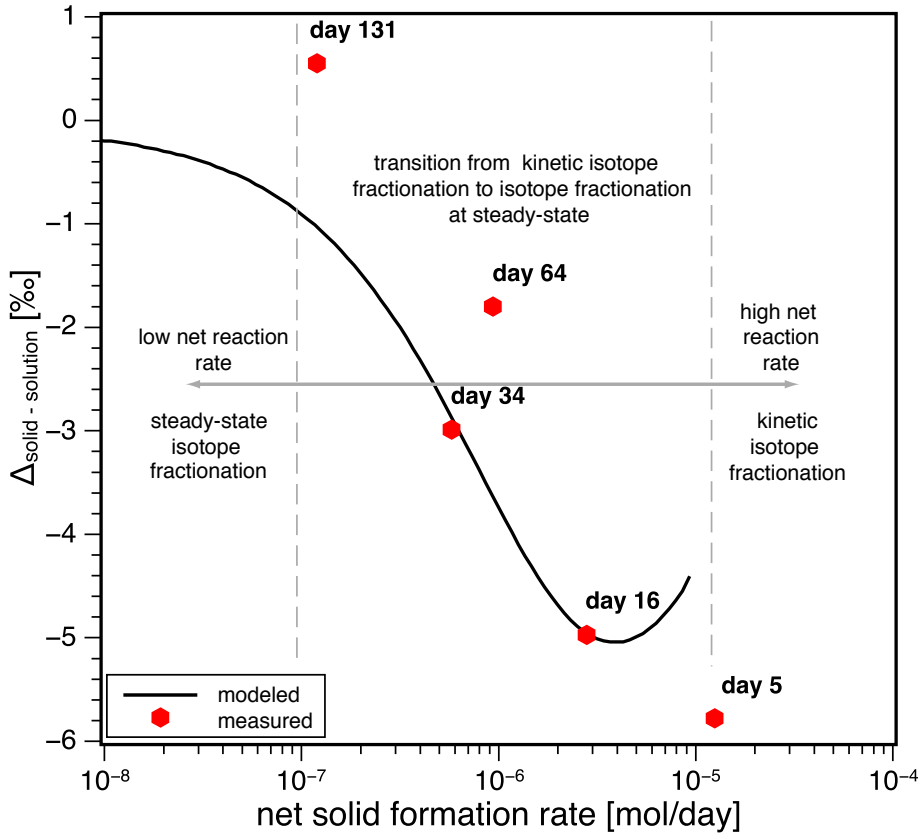

Figure 7: Isotopic difference between solid and solution $\Delta_{solid-solution}$ vs. net solid formation rate. The symbols show the measured $\Delta_{solid-solution}$ at the associated net solid formation rate, calculated from the amounts of Si in the solution and the solid, respectively. The black curve shows a mass balance model of the high-Al freeze-thaw experiment (1 mmol/l; series (c)) at pH 4.5. Shown here is Model 3 calculated from Eqn. B.4 in the Online Supplement B. The early stages of the experiment are dominated by kinetic isotope fractionation, whereas the second stage records isotope fractionation at steady-state with $\Delta_{solid-solution} \cong 0$.

Online Supplement A. Determination of mono-and polysilicic acid using the β-silicomolybdate method

We verified that the Si stock solution contains only monomeric silicic acid by using the β-silicomolybdate method (described in detail by Iler (1982) and Dietzel (2000)). This method is based on the reaction of molybdate with dissolved Si to a yellow colored β-silicomolybdate aquocomplex, detected at 390 nm by spectrometry for 10 min (UV-VIS Cary 100, Varian). The reaction rate constant, k, for the unidirectional reaction of molybdate with dissolved silica, obtained by fitting a second-order reaction, is 2.1 $\pm$0.2 min^{-1} for the prepared solution. This measured range of k values clearly indicates that only monomeric silicic acid, $Si(OH)_4$, is present in solution as polymeric silica induces k values of 0.9, 0.4 and up to 0.030 min^{-1} for dimeric and octameric silica and for silica colloids with about 40 silicon atoms in its structure, respectively (e.g. Iler (1979)).

We also determined the degree of polymerization of some experimental solutions after certain freeze-thaw cycles. The supersaturation during freezing leads to the formation of polysilicic acid even after 1 freeze-thaw cycle. The results are shown in Figure A.2.

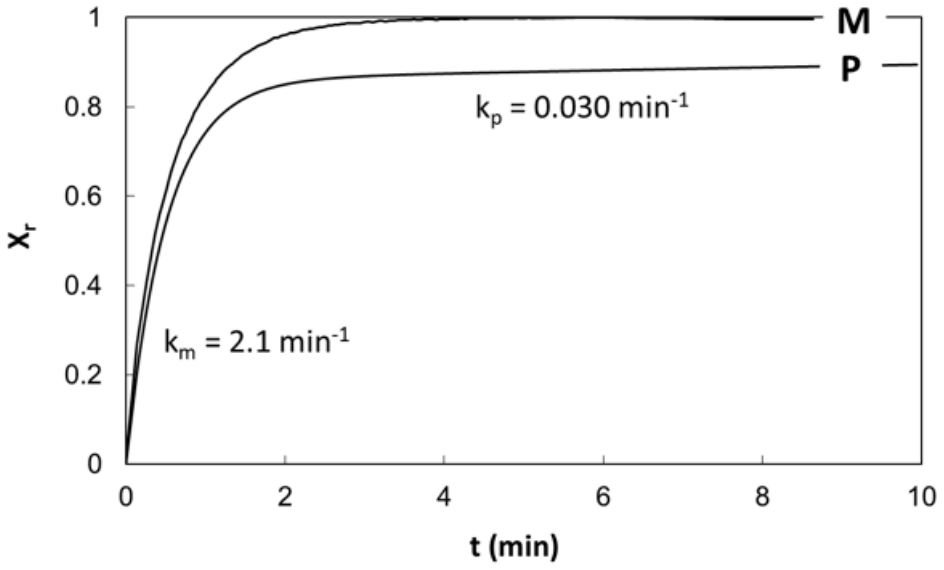

Figure A.1: Evolution of the β-silicomolybdate complex formation in the reaction of molybdate with dissolved Si. t: reaction time of the measurement, X_r: molar fraction of total dissolved Si that has reacted to the silicomolybdate complex (see Dietzel, 2000 for details), M: monosilicic acid stock solution, P: solution containing both monosilicic (86%) and polysilicic acid (14%) (soil solution from Wonisch et al., 2008). Polysilicic acid was not detected in our experimental initial solutions (evolution according to curve M); k_m and k_p denote the reaction rate constant for the reaction of monosilicic and polysilicic acid to the β-complex, respectively.

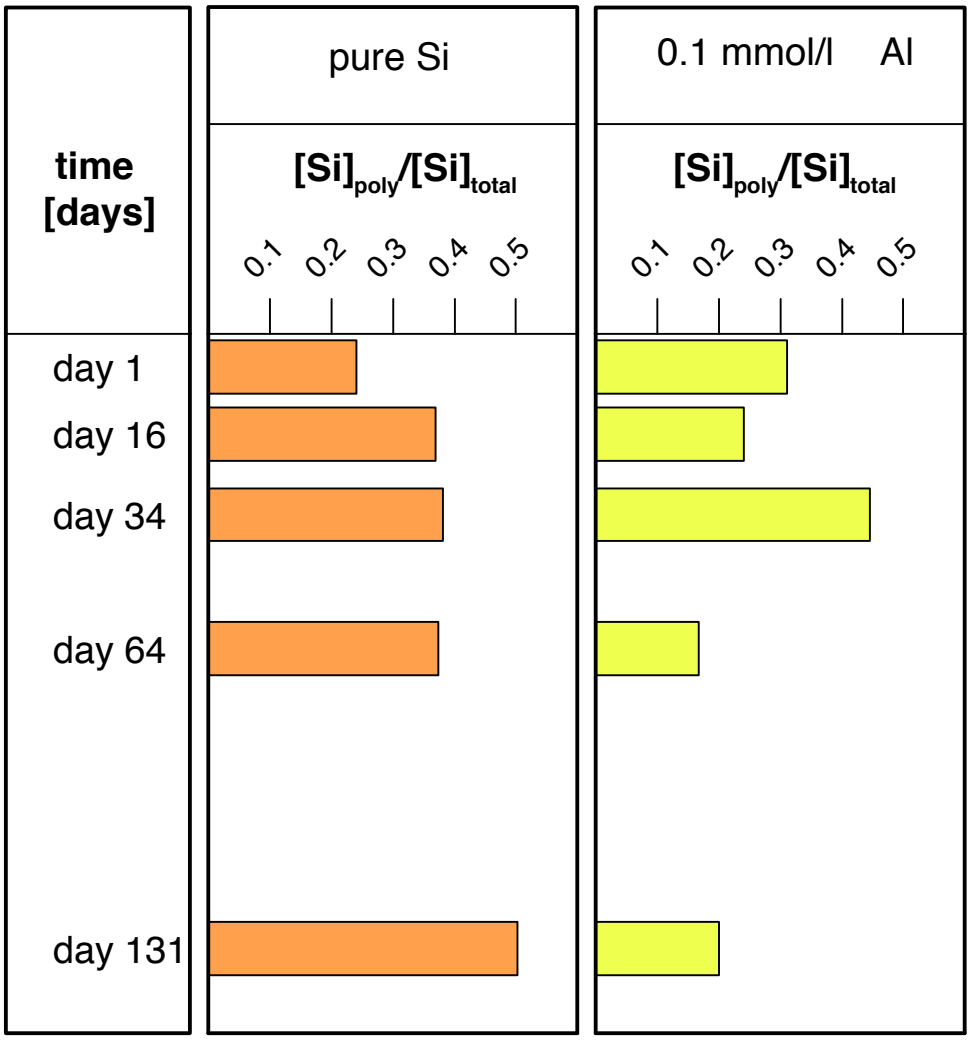

Figure A.2: Degree of polymerization of dissolved silicic acid expressed as the ratio of Si concentration of polysilicic acid ($[\mathrm{Si}]_{\mathrm{poly}}$) to the total amount of dissolved Si ($[\mathrm{Si}]_{\mathrm{total}}$) with and without Al at acidic conditions. The high degree of supersaturation during freezing stages leads to the formation of polysilicic acid already after one freeze-thaw cycle.

Online Supplement B. Modeling a net precipitation-dissolution process associated with isotope fractionation

The aim of this modeling approach is not to determine exact rates or rate constants for attachment or detachment of Si. Determining rate constants would require that conditions (temperature, degree of under- and oversaturation, etc.) and solid properties (surface area) were constant during our experiments. This is not the case here. We rather intend to narrow the range of possible parameters that potentially explain the observed isotopic evolution of Si during our experiments. In order to test whether the experimental kinetics of the freezing-thawing approach can be described as two opposing first-order reactions for net precipitation and net dissolution, we tested several different kinetic rate models (zeroth-order, first-order, second-order, etc.) for the high-Al experiments. The net reaction rate constants used represent parameters that integrate over the changing conditions during the experiments.

First we modeled the evolution of Si concentration. A pure precipitation mechanism following a kinetic rate law of zeroth-order can be dismissed, as the evolution of Si concentration with time clearly shows no linear dependence (see Figure B.1). A pure precipitation mechanism following a first-order kinetic rate law (Eq. B.1) can neither be reconciled with the measured Si concentration data for a best fit through the measured data (see Figure B.1 Model A) nor when we force the model to fit the Si concentration at t=131 days (see Figure B.1 Model B).

$$\frac{d}{dt}(M_d) = F_{prec} = -p \times M_d \tag{B.1}$$

Where M_d is the mass of dissolved Si in the experiment, F_{prec} is the net precipitation of Si and p is the rate constant.

Assuming a second-order kinetic rate law (Eq. B.2) results in a reasonable fit to the measured Si concentration data (see Model C in Figure B.1).

$$\frac{d}{dt}(M_d) = F_{prec} = -p \times M_d^2 \tag{B.2}$$

We next explored whether this second-order precipitation model is compatible with the measured isotope ratios. Unidirectional precipitation without back reaction can be quantified with an open-system mass balance model (Johnson et al., 2004). For the high-Al experiment (1mmol/l Al) at pH 4.5, the open-system model was applied incrementally from sampling point to sampling point. The initial Si concentration and initial isotope composition $\delta(^{30/28}Si)_{initial}$ in solution were those of the previous step. This mass balance calculation shows that the isotope fractionation factors change with each time-step. These isotope fractionation factors $10^3 ln\alpha_{solid/solution}$ are: day0-1: -4.3‰, day1-5: -5.2‰, day8-16: -1.0‰, day16-34: 6.4‰, day34-64: 0.5‰, day64-131: 7.8‰). Isotope fractionation factors for Si as high as 7.8‰ calculated for the final steps have never been observed for Si isotope, and are regarded as highly unlikely. We therefore conclude that unidirectional precipitation is not a feasible mechanism to explain the observed Si isotopic evolution.

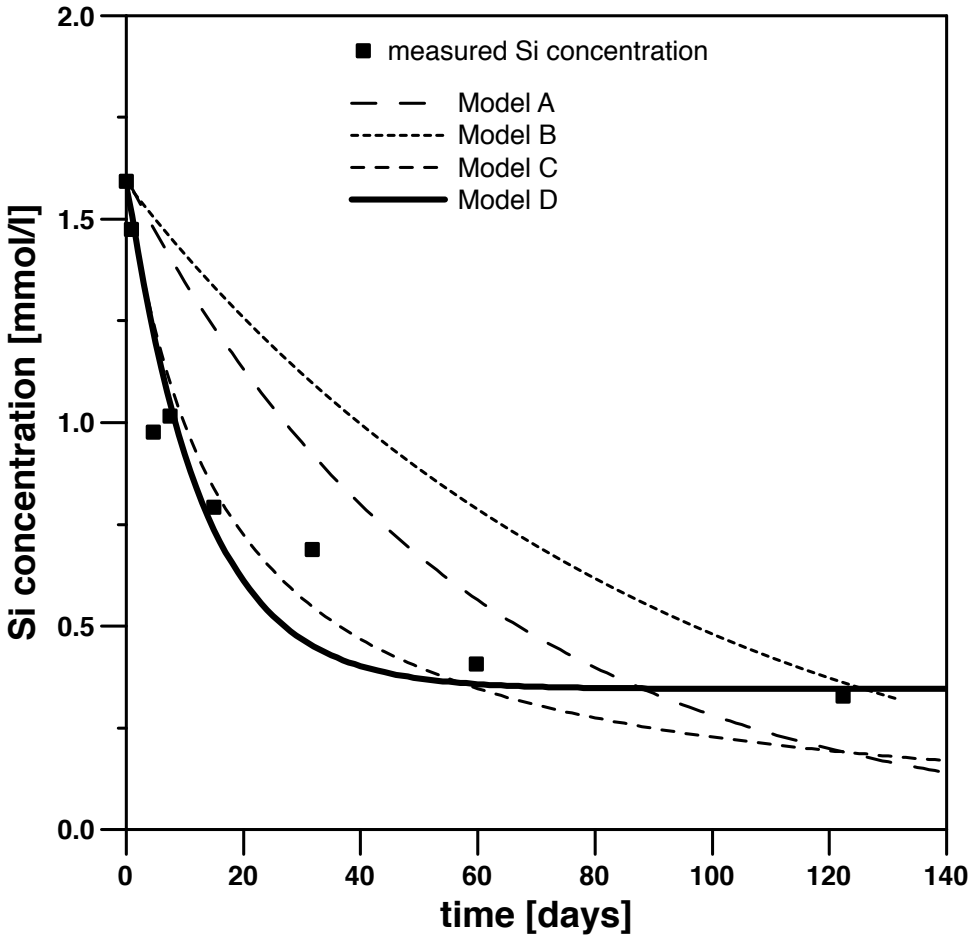

Figure B.1: Model fits using different kinetic rate laws of Si solution concentrations in our high-Al experiments (1 mmol/l al) at pH 4.5. Model A: first-order kinetic rate law for precipitation only, best fit to all measured data; Model B: first-order kinetic rate law for precipitation only, model forced through the Si concentration at t=131 days; Model C: second-order kinetic rate law for precipitation only, best fit to all measured data; Model D: first-order kinetic rate law for precipitation and a first-order kinetic rate law for dissolution, best fit to all measured data.

Therefore we assume that two opposing reactions are in operation, and model these with a first-order kinetic rate law for precipitation and a first-order kinetic rate law for dissolution. In the mass balance equation (Eq. B.3), M_d is the total mass of Si dissolved in solution, M_s is the total mass of Si solid and p and d are net reaction rate constants, p for precipitation and d for dissolution, respectively.

$$\frac{d}{dt}(M_d) = F_{diss} - F_{prec} = d \times M_s - p \times M_d \tag{B.3}$$

Assuming that the dissolved Si concentration at the end of the experiments reflects the steady-state concentration, we can use the steady-state ratio $(M_d/M_s)_{steady-state}$) which equals the d/p ratio (Table B.1), Which reduces the number of adjustable parameters to one.

$$d = p \times \left(\frac{M_d}{M_s}\right)_{steady-state} \tag{B.4}$$

The evolution of M_d (and hence of dissolved Si concentration) was then numerically modeled and fitted to the measured data according to Eq. B.5, using $M_s = M_{total} - M_d$ with M_{total} being the total mass of Si to determine a value for p (Table B.1).

$$\frac{d}{dt}(M_d) = p \times \left(\frac{M_d}{M_s}\right)_{steady-state} \times (M_{total} - M_d) - p \times M_d \tag{B.5}$$

This assumption yields a reasonable fit to the measured Si concentration data (see Model D in Figure B.1).

Next we develop an isotope mass balance model based on these simultaneous first-order kinetic rate laws for precipitation as well as for dissolution. The basic approach is the same for all scenarios explored. First, the evolution of dissolved Si concentration was modeled by using simple first-order irreversible kinetic descriptions of precipitation as well as for dissolution (Eq. B.3). The evolution of the Si isotopic signature was modeled as follows:

$$\frac{d}{dt}(M_d\delta_d) = F_{last} \times (\delta_l + \Delta_{diss}) + F_{cumulative} \times (\delta_c + \Delta_{diss}) - F_{prec} \times (\delta_d + \Delta_{prec}) \quad \text{(B.6)}$$

where Δ_{diss} ($\Delta_{diss} \approx 10^3 ln\alpha_{diss}$) is the kinetic isotope fractionation factor during dissolution and Δ_{prec} ($\Delta_{prec} \approx 10^3 ln\alpha_{prec}$) is the kinetic isotope fractionation factor during precipitation. Here, the solid dissolution flux F_{diss} (Eq. B.1) has been separated into two components: the mass supplied by the outermost layer that precipitated at the previous step F_{last} and the mass from the cumulative solid $F_{cumulative}$ (formed since the beginning of the experiment). Therefore we also make a distinction between the isotopic signature of the outermost ("last") layer δ_l and the isotopic signature of the cumulative solid δ_c. The use of Eq. B.6 allows us to treat the solid as zoned or unzoned. To simplify Eq. B.6 we assume that the end of the experiments represents steady-state. Eq. B.6 dictates that at steady-state $(\delta_s - \delta_d)_{steady-state} = \Delta_{prec} - \Delta_{diss}$, regardless of the value of F_{diss} vs. $F_{cumulative}$. Therefore we constrain the difference $\Delta_{prec} - \Delta_{diss}$ from the isotope data obtained at the end of our experiment (Table B.1). We calculate the relative contribution of the cumulative solid $f_{cumulative}$ to the total

dissolution as:

$$f_{cumulative} = F_{cumulative}/(F_{last} + F_{cumulative}) \quad \text{(B.7)}$$

We then model the measured δ_d values numerically, by using p, d (as previously determined from Si concentrations), and measured $\delta_s - \delta_d$ values from Table B.1 and put them into Eq. B.6. By using these values we fit the model (Eq. B.6) to the transient part of the experimental data by varying Δ_{prec} (hence Δ_{diss}). We repeat the above procedure by incrementally modeling the solid from being isotopically homogeneous ($f_{cumulative} = 1$) to being fully zoned ($f_{cumulative} = 0$). For each of these calculations, we obtain a pair of Δ_{prec} and Δ_{diss} values which is fitted to the measured isotopic evolution of dissolved Si.

In particular we show here the results of the four following models:
Model I and II assume no Si isotope fractionation during dissolution, whereas Model III and IV assume Si isotope fractionation during dissolution. Model I assumes that the solid has a uniform isotopic composition ($f_{cumulative} = 1$), whereas Model II assumes that the isotopic composition of the last precipitated layer reflects the isotopic evolution of the solution with time ($f_{cumulative} = 0$). Hence in this model the solids are assumed to be isotopically zoned and dissolution only redissolves the last precipitated layer. Models III (solid has a uniform isotopic composition) and IV (solid is isotopically zoned) are identical to models I to II, but they further assume that Si isotope fractionation occurs also during solid dissolution. The results of these models are shown for the high-Al experiments in Figures B.2 for the experiment at pH 4.5 and in Figure B.3 for the experiment at pH 7.

Table B.1: Summary of modeling parameters $(M_s/M_d)_{steady-state}$, p, d and $(\delta_s - \delta_d)_{steady-state}$ used in Eq. B.1 and B.4

	$(M_d/M_s)_{steady-state}$	p [day^{-1}]	d [day^{-1}]	$(\delta_s - \delta_d)_{steady-state}$ [‰]
pH4.5/27 ppm Al	0.28	0.06	0.02	0.55
pH7/27 ppm Al	0.02	0.57	0.01	-0.26

For the high-Al experiment (1 mmol/l) at pH 4.5 we find the best fit for an isotopically homogeneous solid ($f_{cumulative} = 1$) with Si isotope fractionation factors of $\alpha^{30/28}Si_{prec} = 0.9953$ ($10^3 ln\alpha_{prec}$ = -4.7‰) and $\alpha^{30/28}Si_{diss} = 0.9947$ ($10^3 ln\alpha_{diss}$ = -5.3‰) .

For the high-Al experiment (1 mmol/l Al) at pH 7 the best fit were obtained either by assuming an isotopically homogeneous solid ($f_{cumulative} = 1$) or a solid comprising a mixture between an isotopically homogeneous solid and the last precipitated layer ($f_{cumulative} = 0.9$ to $f_{cumulative} = 0.5$). All models yielded similar Si isotope fractionation factors of $\alpha^{30/28}Si_{prec} = 0.9989$ to 0.9991 ($10^3 ln\alpha_{prec}$ = -1.1 to -0.9‰) and $\alpha^{30/28}Si_{diss} = 0.9992$ to 0.9994 ($10^3 ln\alpha_{diss}$ = -0.8 to -0.6‰).

The results for both high-Al experiments at pH 4.5 and at pH 7 are:
a) Isotope fractionation during precipitation only (Δ_{prec}) is not the sole cause, as models I to II fail to explain the data, regardless of whether the solid is treated as homogeneous or zoned. In these cases the solution would evolve towards a steady state characterized by high $\Delta(^{30/28}Si)_{solution}$ values, which cannot be reconciled with the data.

b) For the experiment at pH 4.5, only model III assuming two independent fractionation factors, Δ_{prec} during forward reaction and Δ_{diss} during the backward reaction and further assuming an isotopically homogeneous solid ($f_{cumulative} = 1$), yield a reasonable fit to the data.

c) For the experiment at pH 7, models between $f_{cumulative} = 1$ and $f_{cumulative} = 0.5$ assuming two independent fractionation factors, Δ_{prec} during forward reaction and Δ_{diss} during the backward reaction yield reasonable fits to the data.

c) The models in which only the outermost layer of zoned solids is dissolved (Model II and Model IV) do not yield results that can be reconciled with the data, even when applying two different fractionation factors (Δ_{prec} & Δ_{diss}). It follows that the major part, or even the entire solid is homogenized during the course of the experiment, presumably due to redissolution. In Tables B.2 and B.3, the best-fit values for the described models I to VI for the high Al experiments are presented.

To conclude, for the high Al experiments the major part of the formed solid is redissolved and exchanges with the solution. The best fit values of the isotope fractionation factors associated with precipitation are similar to those of dissolution and are $\alpha^{30/28}Si_{prec}$ =0.9953 ($10^3 ln\alpha_{prec}$ = -4.7‰) and $\alpha^{30/28}Si_{diss}$ =0.9947 ($10^3 ln\alpha_{diss}$ = -5.3‰) for the experiment at pH=4.5 and $\alpha^{30/28}Si_{prec}$ =0.9989 to 0.9991 ($10^3 ln\alpha_{prec}$ = -1.1 to -0.9‰) and $\alpha^{30/28}Si_{diss}$ =0.9992 to 0.9994 ($10^3 ln\alpha_{diss}$ = -0.8 to -0.6‰) for the experiment at pH=7.

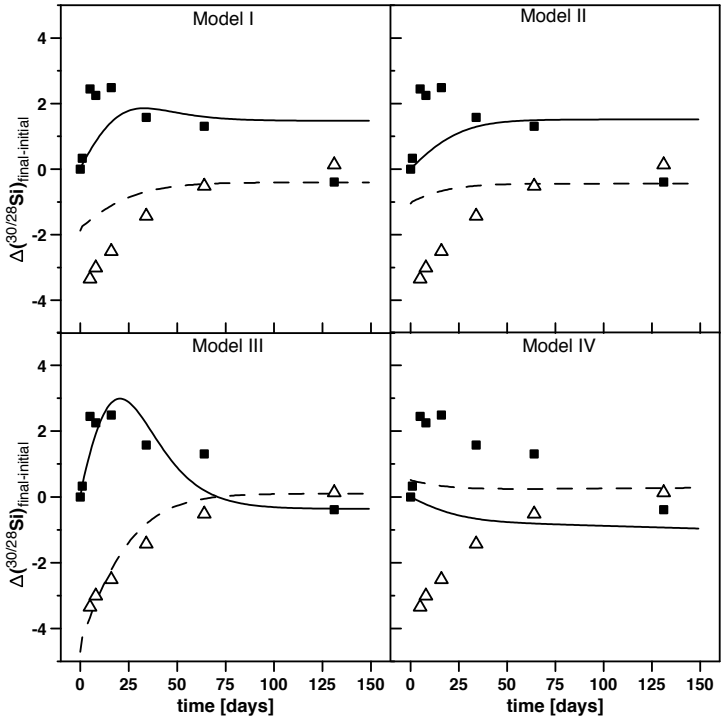

Figure B.2: Modeled evolution of Si isotope composition in solutions and solids with time and comparison with data for the high-Al experiment (1 mmol/l Al) at pH 4.5. Modeled curves for the solution (black line) and solid (dashed line) are fitted to measured data. Squares depict measured solution and triangles depict the corresponding solid, respectively. Only Model III, assuming unzoned solids, yield reasonable fits to the data.

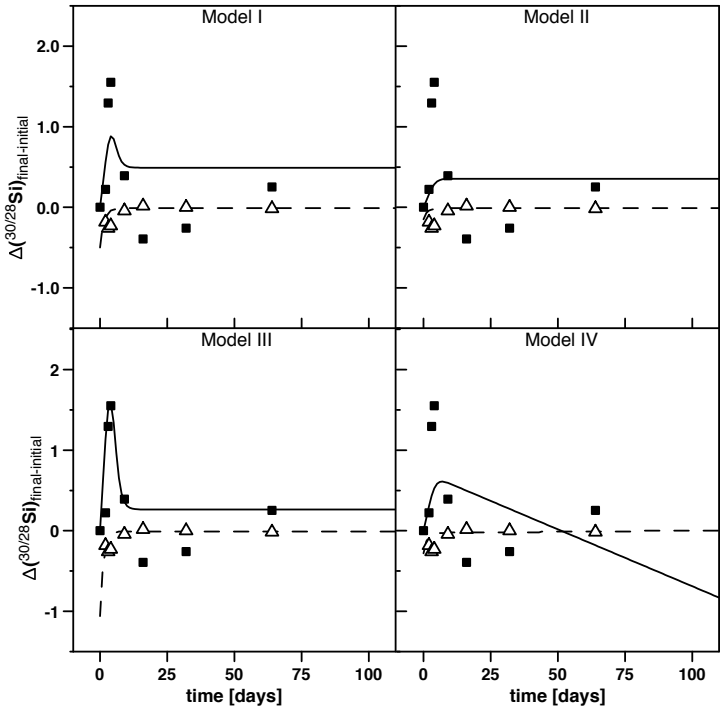

Figure B.3: Modeled evolution of Si isotope composition in solutions and solids with time and comparison with data for the high-Al experiment (1 mmol/l Al) at pH 7. Modeled curves for the solution (black line) and solid (dashed line) are fitted to measured data. Squares depict measured solution and triangles depict the corresponding calculated solid, respectively. Only Model III, assuming unzoned solids, yield reasonable fits to the data.

Table B.2: Best fit values of Eq. B.6 for the modeled curves in Figure B.2 for the high-Al experiment (1 mmol/l Al) at pH 4.5.

	Δ_{prec} [‰]	Δ_{diss} [‰]	$f_{cumulative}$	f_{last}	RMSD[a]
Model I	-1.9	0.00	1.0	0.0	1.2
Model II	-1.1	0.00	0.0	1.0	1.4
Model III	-4.7	-5.3	1.0	0.0	0.7
Model IV	0.5	0.0	0.0	1.0	2.0

[a]root-mean-square deviation (RMSD) where y is the regression dependent variable, $\hat{y}$ is the predicted variable and n is the number of predictions; is calculated as follow:

$$RMSD = \sqrt{\frac{\sum_{t=1}^{n}(y_t - \hat{y}_t)^2}{n}}$$

Table B.3: Best fit values of Eq. B.6 for the modeled curves in Figure B.3 for the high-Al experiment (1 mmol/l Al) at pH 7.

	Δ_{prec} [‰]	Δ_{diss} [‰]	$f_{cumulative}$	f_{last}	RMSD[a]
Model I	-0.5	0.0	1.0	0.0	0.6
Model II	-0.2	0.0	0.0	1.0	0.75
Model III	-1.1	-0.8	1.0	0.0	0.3
Model IV	-0.3	0.0	0.0	1.0	0.7

[a]root-mean-square deviation (RMSD) where y is the regression dependent variable, $\hat{y}$ is the predicted variable and n is the number of predictions; is calculated as follow:

$$RMSD = \sqrt{\frac{\sum_{t=1}^{n}(y_t - \hat{y}_t)^2}{n}}$$

References

Dietzel, M. (2000). Dissolution of silicates and the stability of polysilicic acid. Geochimica et Cosmochimica Acta, 64(19), 3275-3281.

Iler, R. K. (1979). The chemistry of silica: solubility, polymerization, colloid and surface properties, and biochemistry. New York: John Wiley & Sons, Inc.

Johnson, C. M., Beard, B. L., & Albarede, F. (2004). Overview and general concepts. Reviews in Mineralogy and Geochemistry, 55, 1-24.

Wonisch, H., Gerard, F., Dietzel, M., Jaffrain, J., Nestroy, O., & Boudot, J. P. (2008). Occurrence of polymerized silicic acid and aluminum species in two forest soil solutions with different acidity. Geoderma, 144(3-4), 435-445.